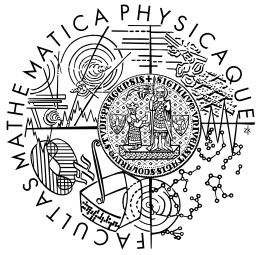

FACULTY
OF MATHEMATICS
AND PHYSICS
Charles University

MASTER THESIS

Bc. Karel Pajskr

Magnetic properties of Nd_2RhIn_8 and related tetragonal Nd-based compounds

Department of Condensed Matter Physics

Supervisor of the master thesis: Doc. Mgr. Pavel Javorský, Dr.

Study programme: Fyzika (N1701)

Study branch: FKSM (1701T041)

Prague 2016

I declare that I carried out this master thesis independently, and only with the cited sources, literature and other professional sources.

I understand that my work relates to the rights and obligations under the Act No. 121/2000 Sb., the Copyright Act, as amended, in particular the fact that the Charles University has the right to conclude a license agreement on the use of this work as a school work pursuant to Section 60 subsection 1 of the Copyright Act.

In ..... date ..... signature of the author

Title: Magnetic properties of Nd_2RhIn_8 and related tetragonal Nd-based compounds

Author: Bc. Karel Pajskr

department: Department of Condensed Matter Physics

Supervisor: Doc. Mgr. Pavel Javorský, Dr., Department of Condensed Matter Physics

Abstract: In this work we report on physical properties of Nd_2RhIn_8 and Nd_2IrIn_8 rare-earth intermetallic compounds from the $R_mT_nX_{2n+3m}$ compound family. The compounds crystallize in the *P4/mmm* space group. Both compounds are antiferromagnetic with Néel temperatures T_N of 10.8 K, 12.5 K respectively and their magnetization curves show characterisic step-like transitions at low temperatures. The measured $M(T)$ and/or $M(H)$ magnetization curves were used to determine magnetic phase diagrams for field along the *c*-axis. The specific heat of Nd_2IrIn_8 was analyzed at temperatures $T<T_N$ with respect to the dimensionality of the magnetic excitations. In the $T>T_N$ region the Schottky specific heat and susceptibility were compared to calculations based on the crystal field scheme in Nd_2IrIn_8 obtained by ab-initio methods.

Keywords: rare-earth compounds, magnetic phase diagram, crystal field

Název práce: Magnetické vlastnosti Nd_2RhIn_8 a příbuzných tetragonálních sloučenin na bázi Nd

Autor: Bc. Karel Pajskr

Katedra: Katedra fyziky kondenzovaných látek

Vedoucí diplomové práce: Doc. Mgr. Pavel Javorský, Dr., Katedra fyziky kondenzovaných látek

Abstrakt: Tématem předkládané práce je studium fyzikálních vlastností vzácnozeminných intermetalik Nd_2RhIn_8 a Nd_2IrIn_8 z rodiny sloučenin $R_mT_nX_{2n+3m}$. Studované sloučeniny krystalizují ve struktuře *P4/mmm*. Obě látky jsou antiferomagnetiky s Néelovými teplotami T_N 10.8 K, resp. 12.5 K a jejich magnetizační křivky za nízkých teplot vykazují charakteristické, dobře ohraničené přechody. Změřené magnetizační křivky $M(H)$ a $M(T)$ byly použity pro odvození magnetických fázových diagramů těchto sloučenin pro magnetické pole podél osy *c*. Dále bylo analyzováno měrné teplo sloučeniny Nd_2IrIn_8, a to v oblasti $T<T_N$ s ohledem na dimenzionalitu magnonové excitace. Pro teploty $T>T_N$ bylo Schottkyho měrné teplo a křivky susceptibilit srovnány s výpočty z krystalovopolních parametrů, které byly získány pomocí ab-initio metod.

Klíčová slova: vzácnozeminné sloučeniny, magnetický fázový diagram, krystalové pole

I would like to express my thanks and dedicate this work to my supervisor Doc. Pavel Javorský, Dr. from the Department of Condensed Matter Physics of the Charles University in Prague. He was always unbelievably helpful and gave me lots of beneficial advice. Only thanks to him and his patience I was able to finish this thesis at last.

I am thankful to Ing. Eva Šantavá, CSc., RNDr. Vladimír Tkáč, RNDr. Róbert Tarasenko and the members of the MLMT staff for their support and guidance during my measurement time on PPMS and MPMS systems and to Doc. Martin Diviš for the ab-initio calculations.

I would like to thank RNDr. Marie Kratochvílová, Honza Zubáč and Kristina Vlášková for their help with sample preparation and measurements, not mentioning many friendly discussions (not exclusively) about Physics.

Lastly, I would like to thank my beloved parents for everything, they will always mean the world to me.

Contents

1. Introduction

Due to many interesting and specific properties which can lead to applications in industry and engineering as well as to new developments of the theory, the study of lanthanide and actinide based intermetallic compounds and their magnetic properties became one of the standard topics in the broad field of condensed matter physics. The contrast between the localized $4f$ electrons residing deep in the atomic shell and the itinerant character of the d electrons symbolizes one of the main difficulties of the theory of magnetism. This thesis deals mostly with the first aspect as, in our case, it was the adequate framework to describe the magnetic phenomena in the studied compounds.

In this work I present a study of sample preparation and measurements of physical properties of tetragonal Nd-based intermetalic compounds Nd_2RhIn_8 and Nd_2IrIn_8. Nd-based compounds were chosen due to a close relation between neodymium and cerium. The compounds belong to a large structurally related compound family whose formula can be written as $R_mT_nX_{2n+3m}$.

After the introductory chapter, a brief overview of the theoretical description of the observed physical phenomena is presented in the second chapter. The third chapter is an introduction to the methods and techniques that were used for the calculations and measurements. The main part of the thesis, the fourth chapter, then gives a presentation of the results obtained during the experiments, derived results and their discussion which is followed by a short conclusion chapter.

1.1 $R_mT_nX_{2n+3m}$ compounds

$R_mT_nX_{2n+3m}$ (R = rare earth, T = late transition metal, X = In or Ga) form a large group of compounds whose structure consists of m RX_3 and n TX_2 building blocks stacked sequentially along the c-axis. The most studied members of the group have the stoichiometries of 1-3 (1-0-3), 1-1-5 and 2-1-8[1]. The number of TX_2 layers has a profound effect on the dimensionality of the rare earth ions which moves from purely 3D in 1-3 to a partially quasi-2D character in the other variants and provides a great possibility for a systematic study of physical properties as a function of both composition and dimensionality. The structure of the compounds is shown in Fig. 1.1. The 1-1-5 and 2-1-8 compounds crystallize in the $HoCoGa_5$ and Ho_2CoGa_8 tetragonal structures, space group $P4/mmm$ (No. 123). The 1-3 compound in the $AuCu_3$ cubic structure, $Pm\bar{3}m$ (No. 221).

The cerium (R = Ce) based $R_mT_nX_{2n+3m}$ compounds have been studied during recent years due to their unique and intriguing properties such as heavy-fermion (HF) superconductivity, interplay between magnetic order and superconductivity or quantum criticality [3, 4]. As it is believed that those properties have a close relation to the magnetic interactions of the systems, studies which replace cerium with another rare-earth ion are often used to separately study the underlying RKKY interaction and crystalline electric field (CEF or CF). In next paragraph I give an overview of related Ce-based compounds with a mention of their main properties.

[1] other known stoichiometries are 3-1-11, 5-2-19 [1] or 1-2-7 [2].

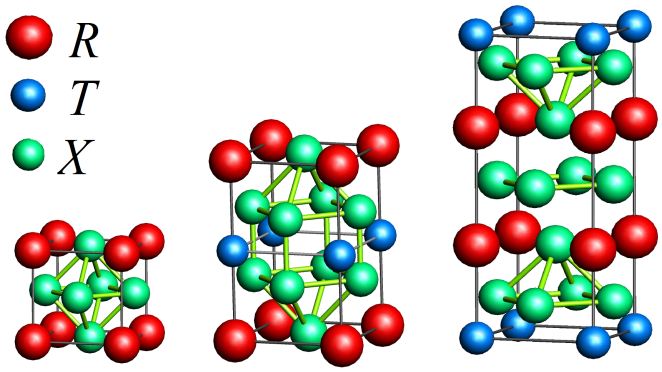

Figure 1.1: Structure of the '1-3', '1-1-5' and '2-1-8' compounds. The structure is built by repeating RX_3 and TX_2 blocks. The '2-1-8' structure can be viewed as a RX_3 unit cell sandwitched between two TX_2 layers.

Ce_2RhIn_8 and $CeRhIn_5$ are antiferromagnets with $T_N = 2.8\,K$ and $T_N = 3.8\,K$ and become superconducting at $T_{SC} = 0.4\,K$ and $T_{SC} = 2.2\,K$ under applied pressures of 1.1 GPa and 1.63 GPa respectively [5, 6]. Ce_2IrIn_8 is a HF paramagnet and does not undergo any superconducting transition at known temperatures [7]. $CeIrIn_5$ is a HF superconductor with transition temperature of $T_{SC} = 0.4\,K$ [8]. The cubic relative, $CeIn_3$ is an antiferromagnet with $T_N = 10\,K$ [9] that becomes superconductive at $T_{SC} = 0.18\,K$ under the applied pressure of 2.8 GPa [10].

Evolution of the Néel temperature across the rare earth group for the 1-3, 1-1-5 and 2-1-8 compounds with $T = Rh$ and $X = In$ is shown in Fig 1.2 and visually compared to the scalling proportional to the de Gennes factor $(g-1)^2 J(J+1)$. The effect of the so called lanthanide contraction is visible in Fig 1.3 which shows the dimensions of the unit cells of the R_2RhIn_8 compounds.

The commonly observed behaviour of magnetic properties in the compound family is shown in Figs. 1.4 and 1.5 which show the characteristic step-like transitions often present in magnetization curves and the influence of the crystal field on the curvature of the susceptibility curves. Fig. 1.5 shows the magnetization curves of Ho_2RhIn_8 and Er_2RhIn_8 which differ in the orientation of the easy magnetization direction ([001] for $R = Ho$, [110] for $R = Er$).

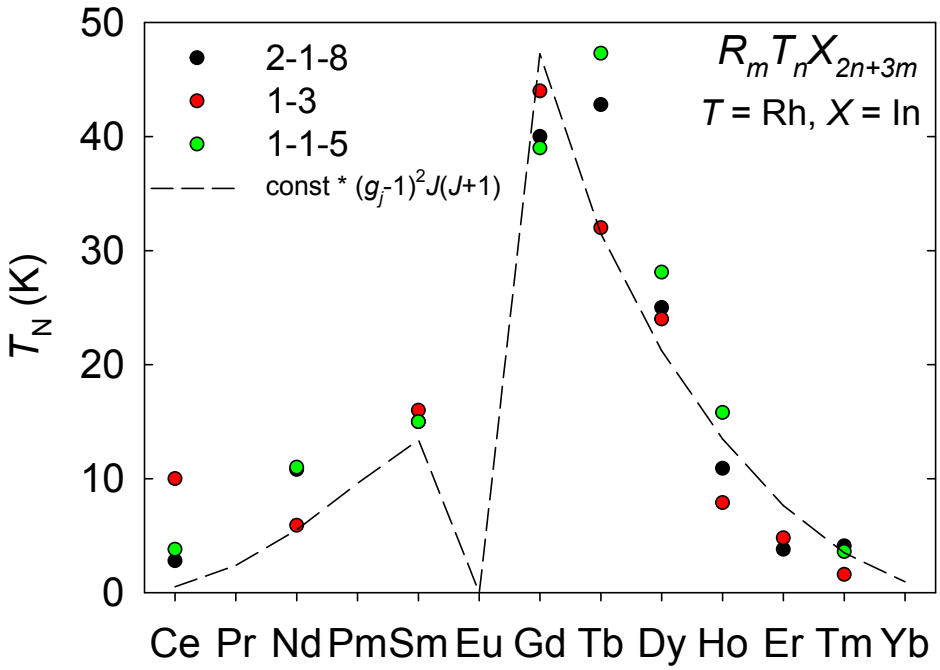

Figure 1.2: Néel temperature scalling among the compound family for T = Rh, X = In compared to the size of the de Gennes factor. The line is a guide to the eye. Sources: [5, 6, 9] (Ce), [11, 12] (Nd), [13, 14] (Sm), [13, 14] (Gd), [15, 16] (Tb), [16–18] (Dy), [16, 17, 19] (Ho), [16, 17, 19] (Er), [16, 17, 20] (Tm)

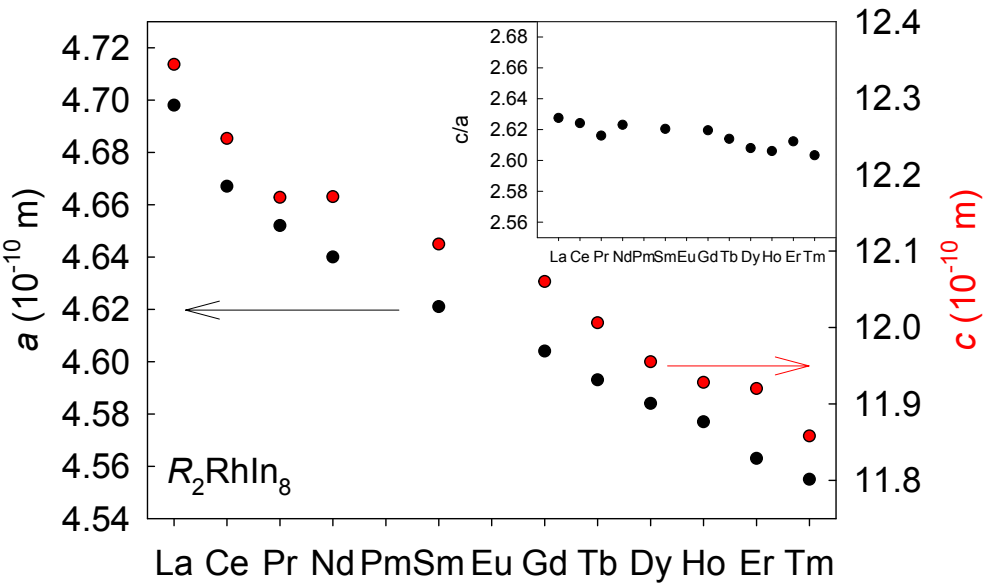

Figure 1.3: Lanthanide contraction in the R_2RhIn_8 compounds. Sources: [12, 13, 16, 21, 22]

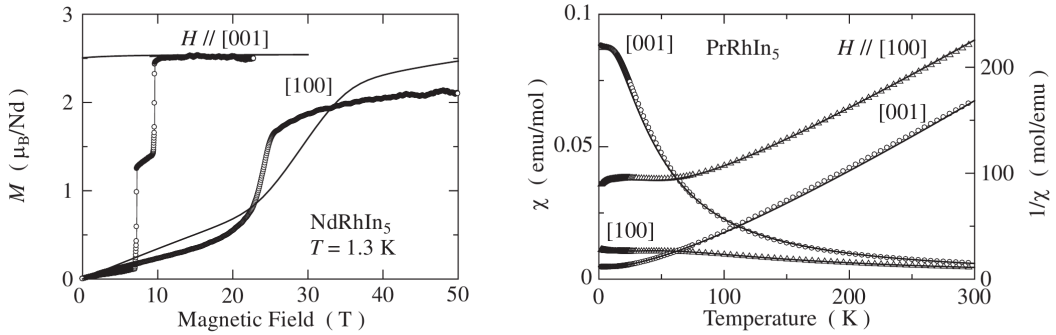

Figure 1.4: Characteristic curves for $R_mT_nX_{2n+3m}$ - step-like transitions and influence of the crystal field. Taken from Ref. [17].

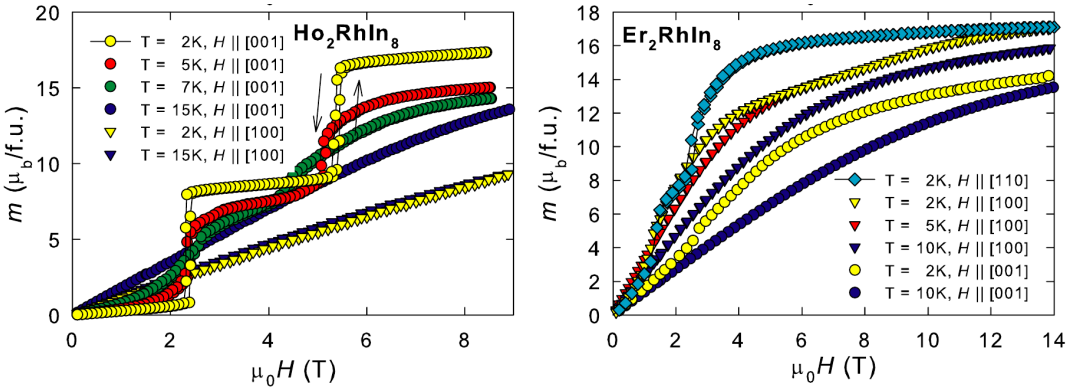

Figure 1.5: Characteristic step-like transitions at low temperatures in the magnetization of $R_mT_nX_{2n+3m}$ compounds. Taken from Ref. [16].

2. The Physics of Rare-earth Intermetallic Compounds

2.1 Magnetism

2.1.1 Main concepts

Classical physics defines the *magnetic dipole moment* as

$$\boldsymbol{m} = \frac{1}{2}\int_V [\boldsymbol{r}' \times \boldsymbol{j}(\boldsymbol{r}')]\,\mathrm{d}V\,, \tag{2.1}$$

where $\boldsymbol{r}'$ is the position vector, $\boldsymbol{j}$ is the current density and the integration is over volume V. In the case of a small current loop with current I and area $\boldsymbol{S}$, this can be written as $\boldsymbol{m} = I\boldsymbol{S}$. The SI unit is Am^2 but as we will see later it is more convenient to use the Bohr magneton $\mu_\mathrm{B} = \frac{e\hbar}{2m_e} = 9.274 \cdot 10^{-24}\,\mathrm{JT}^{-1}$ as the unit on the atomic scale[1]. Looking at the value of the Bohr magneton[2] from the energy point of view, it is possible to presume a certain delicacy in localised-magnetism phenomena, often requiring low temperatures and/or relatively high magnetic fields.

Magnetization M is then defined as the sum of magnetic moments per unit volume, mass or formula.

Susceptibility χ, the quantity which relates the magnetic response of a system to the applied field H is defined by

$$\chi = \frac{\partial M}{\partial H}\,. \tag{2.2}$$

For laboratory magnetic fields[3], the $M(H)$ dependence tends to be linear over a broad region so usually one can write $M = \chi H$.

As follows from the Bohr-van Leeuven theorem[4], the combination of classical mechanics and statistical physics does not allow for magnetic phenomena, ie. a thermally averaged moment is always zero according to classical physics. This forces us to move from the classical description to a quantum one.

The magnetic moment of a free atom or ion is caused mainly by the spin of its electrons and by their angular momentum. One can easily derive that a new term $\Delta\hat{\mathcal{H}}$ emerges in the atomic Hamiltonian when a magnetic field of induction $\boldsymbol{B} = \mu_0\boldsymbol{H}$ is applied:

$$\Delta\hat{\mathcal{H}} = \mu_\mathrm{B}\left(\hat{\boldsymbol{L}} + g\hat{\boldsymbol{S}}\right)\cdot\boldsymbol{B} + \frac{e^2}{8m_e}\sum_{i=1}^{n}(\boldsymbol{B}\times\hat{\boldsymbol{r}}_i)\,, \tag{2.3}$$

where $g \approx 2$ is the electron g-factor and $\hat{\boldsymbol{S}}$, $\hat{\boldsymbol{L}}$ is the total spin and angular momentum operator respectively. In this thesis, the dimensionless[5] $\hat{\boldsymbol{S}}$, $\hat{\boldsymbol{L}}$ and

[1] e is the elem. charge, m_e mass of electron, $\hbar$ reduced Planck constant

[2] $\mu_\mathrm{B} \doteq 0.1\,\mathrm{meV.T^{-1}}$, $\frac{1\,\mathrm{meV}}{k_B} \doteq 11\,\mathrm{K}$

[3] up to roughly 10 T.

[4] from 1911.

[5] with integral or half-integral eigenvalues

$\hat{\boldsymbol{J}} = \hat{\boldsymbol{S}} + \hat{\boldsymbol{L}}$ [23] are used instead of the conventional definition. Using the second-order perturbation theory and its adjustment of the energy levels

$$\Delta E_n = \langle n|\Delta\hat{\mathcal{H}}|n\rangle + \sum_{n'\neq n} \frac{\langle n|\Delta\hat{\mathcal{H}}|n'\rangle^2}{E_n - E_{n'}} \tag{2.4}$$

($|n\rangle$, E_n denote unperturbed eigenstates and their energies) we arrive at an important result of the theory of susceptibility of an individual or weakly interacting atom, ion or molecule:

$$\begin{aligned}\Delta E_n = \mu_\mathrm{B}\boldsymbol{B}\cdot\langle n|\hat{\boldsymbol{L}} + g\hat{\boldsymbol{S}}|n\rangle + \sum_{n'\neq n} \frac{\langle n|\mu_\mathrm{B}\boldsymbol{B}\cdot\left(\hat{\boldsymbol{L}} + g\hat{\boldsymbol{S}}\right)|n'\rangle^2}{E_n - E_{n'}} \\ + \frac{e^2}{8m_e}B^2\langle n|\sum_i\left(\hat{x}_i^2 + \hat{y}_i^2\right)|n\rangle\,.\end{aligned} \tag{2.5}$$

With the energy levels, the susceptibility can be calculated using the statistical mechanics as

$$\chi = -\frac{1}{V}\frac{\partial^2 F}{\partial H^2}\,, \tag{2.6}$$

where V is the volume and F is the Helmholz free energy of the system defined as

$$F = -k_\mathrm{B}T\cdot\ln Z\,, \tag{2.7}$$

Z being the partition function of the system $Z = \sum_n e^{-\frac{E_n(H)}{k_\mathrm{B}T}}$ and k_B the Boltzmann constant.

Diamagnetism

In the case of an ion with all electronic shells filled, the ground state $\big|0\big\rangle$ of such ion is characterised by zero total, angular and spin moment

$$\hat{\boldsymbol{J}}\big|0\big\rangle = \hat{\boldsymbol{L}}\big|0\big\rangle = \hat{\boldsymbol{S}}\big|0\big\rangle = 0. \tag{2.8}$$

Then from the last part of the formula (2.5), one can derive the susceptibility

$$\chi_{dia} = -\frac{N}{V}\frac{e^2\mu_0}{6m_\mathrm{e}}\sum_{i=1}^{n}\langle r_i^2\rangle\,, \tag{2.9}$$

which will always be negative. The N, V denote number of ions and volume, μ_0 is the vacuum permeability. Such mode of behavior that a substance is nonmagnetic in the absence of field and has a negative susceptibility in applied field is called diamagnetism. Examples of diamagnetism are represented by inert gasses, Cu or H_20 with $\chi_{dia}^{SI} \doteq 10^{-5}$. Due to the Meissner effect of the expulsion of the magnetic field, materials in superconductive state can be regarded as perfect diamagnets with $\chi_{dia} = -1$. Apart from those, the most diamagnetic material known is the pyrolitic[6] graphite with $\chi_{dia} \doteq 10^{-4}$, one of the few substances which can be used to demonstrate diamagnetic levitation without superconductors.

[6] graphite produced under high temperatures and pressures.

Paramagnetism

Ions with unfilled shells will have non-zero $\boldsymbol{L}$ or $\boldsymbol{S}$. This means that the ion can have nonzero $\boldsymbol{J}$ and its own magnetic moment. If we do not consider any interaction between individual ions, the net magnetization of a material will be determined only by the temperature and the applied field: in zero field the moments will be randomly oriented generating a zero total magnetization. The higher the applied field will be, the more of them will orient themselves along its direction, while higher temperatures will have the opposite effect on magnetization by randomizing the orientations of the moments and lowering their net sum. Taking the quantum-mechanical nature of the effect into account and using statistical mechanics, one arrives at the formula for magnetization of n moments per unit volume

$$M = n g_J \mu_\mathrm{B} J B_J(y), \tag{2.10}$$

given by the Brillouin function $B_J(y)$

$$B_J = \frac{2J+1}{2J} \coth\left(\frac{2J+1}{2J} y\right) - \frac{1}{2J} \coth\frac{y}{2J} \tag{2.11}$$

(Fig. 2.1) with a parameter

$$y = \frac{g_J \mu_\mathrm{B} J B}{k_\mathrm{B} T}, \tag{2.12}$$

where g_J is the Landé g-factor

$$g_J = \frac{3}{2} + \frac{S(S+1) - L(L+1)}{2J(J+1)}, \tag{2.13}$$

where S, L and J denote corresponding quantum numbers. The factor originates from the fact that the spin and angular momentum of an electron have different gyromagnetic ratios so the ion's magnetic moment is not parallel to the total moment $\boldsymbol{J}$ and has to be projected to it and, subsequently, to the direction of the applied field to get its contribution to the magnetization. For small values of y, the Brillouin function can be aproximated as linear and the susceptibility becomes

$$\chi_\mathrm{para} = \frac{C}{T}, \tag{2.14}$$

where

$$C = \frac{n \mu_0 \mu_\mathrm{eff}^2}{3 k_\mathrm{B}}. \tag{2.15}$$

The μ_eff used in the equation is the effective magnetic moment defined by

$$\mu_\mathrm{eff} = g_J \mu_\mathrm{B} \sqrt{J(J+1)} \tag{2.16}$$

Further increasing of the magnetic field results in a maximal orientation of all moments along the field direction and reaching the saturation magnetization M_s:

$$M_s = n g_J \mu_\mathrm{B} J. \tag{2.17}$$

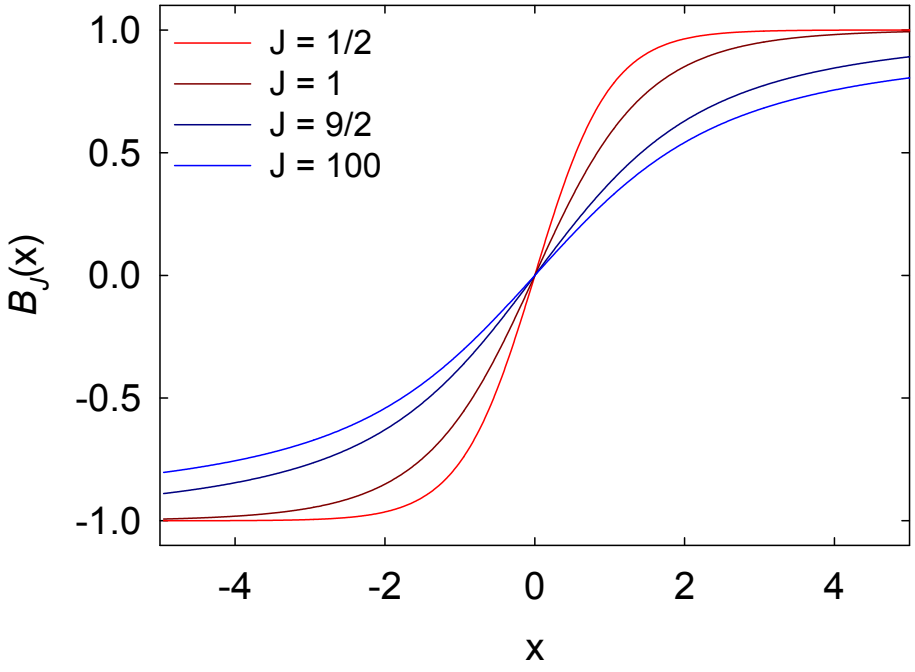

Figure 2.1: Brillouin function for different values of J.

2.1.2 Localised and Itinerant Limits of Behavior

Localised Magnetism Model

The $4f$ electrons' wave functions are localised deep in the atomic shell and have only a negligible overlap which means that they take little part in chemical bonding or contribute to conduction electrons. The important effects which affect the behavior of the $4f$ electrons can be written in the free-ion Hamiltonian $\hat{\mathcal{H}}$ and can be understood as gradual[7] corrections

$$\hat{\mathcal{H}} = \hat{\mathcal{H}}_0 + \hat{\mathcal{G}} + \hat{\mathcal{H}}_{\mathrm{SO}} + \hat{\mathcal{H}}_{\mathrm{CF}}, \tag{2.18}$$

where

$$\hat{\mathcal{H}}_0 = \sum_{i=i}^{N} \left(-\frac{\hbar^2}{2m_{\mathrm{e}}} \nabla_i^2 - Z\frac{e'^2}{r_i} + V_{\mathrm{ef}}(r_i) \right), \; e'^2 = \frac{e^2}{4\pi\epsilon_0} \tag{2.19}$$

(ϵ_0 is the vacuum permitivity) represents the kinetic energy of the electrons, the potential energy of the electron-nucleus system and the effective one-electron potential arising from the Coulomb and exchange interaction. The one-electron solutions of this Hamiltonian are

$$\psi_{nlm}(\boldsymbol{r}) = R_{nl}(r)\, Y_{lm}(\vartheta, \varphi), \tag{2.20}$$

where R_{nl} is a radial function and Y_{lm} is a spherical harmonic and n, l, m denote the principal, orbital angular momentum and magnetic quantum numbers.

[7] assuming the Russel-Saunders approximation and weak crystal field.

R	Ce	Pr	Nd	Pm	Sm	Eu	Gd	Tb	Dy	Ho	Er	Tm	Yb
$4f^N$	$4f^1$	$4f^2$	$4f^3$	$4f^4$	$4f^5$	$4f^6$	$4f^7$	$4f^8$	$4f^9$	$4f^{10}$	$4f^{11}$	$4f^{12}$	$4f^{13}$
ground state	${}^2\mathrm{F}_{\frac{5}{2}}$	${}^3\mathrm{H}_4$	${}^4\mathrm{I}_{\frac{9}{2}}$	${}^5\mathrm{I}_4$	${}^6\mathrm{H}_{\frac{5}{2}}$	${}^7\mathrm{F}_0$	${}^8\mathrm{S}_{\frac{7}{2}}$	${}^7\mathrm{F}_6$	${}^6\mathrm{H}_{\frac{15}{2}}$	${}^5\mathrm{I}_8$	${}^6\mathrm{I}_{\frac{15}{2}}$	${}^3\mathrm{H}_6$	${}^2\mathrm{F}_{\frac{7}{2}}$
g_J	$\frac{6}{7}$	$\frac{4}{5}$	$\frac{8}{11}$	$\frac{3}{5}$	$\frac{2}{7}$	0	2	$\frac{3}{2}$	$\frac{4}{3}$	$\frac{5}{4}$	$\frac{6}{5}$	$\frac{7}{6}$	$\frac{8}{7}$
$\mu_{\mathrm{eff}}^{\mathrm{calc}}$	2.54	3.56	3.62	2.68	0.84	0	7.94	9.72	10.63	10.60	9.59	7.57	4.54

Table 2.1: Ground state multiplets obtained by Hund's rules for the R^{3+} ions.

The solutions[8] form a Slater determinant and in case of $4f$ electrons the ground state has a degeneration of $\binom{14}{N}$ where N is the number of electrons in the shell.

The next term $\hat{\mathcal{G}}$

$$\hat{\mathcal{G}} = \sum_{i<j}^{N} \frac{e'^2}{|\boldsymbol{r}_i - \boldsymbol{r}_j|} - \sum_{i=1}^{N} V_{\mathrm{ef}}(r_i), \tag{2.21}$$

represents the correlation energy of the electrons' movement and can be treated as a perturbation and causes the energy levels split into *terms*, defined by a combination of S and L. As the energy does not depend on quantum numbers L_z or S_z, the $(2S+1)(2L+1)$ degenerate microstates are characterised by quantum numbers L, S, L_z and S_z.

If we assume a small spin-orbit interaction compared to the correlation, the orbital as well as the spin momenta can be summed into $\boldsymbol{L}$, $\boldsymbol{S}$ and the interaction written as

$$\hat{\mathcal{H}}_{\mathrm{SO}} = \lambda(LS)\hat{\boldsymbol{L}}\hat{\boldsymbol{S}}, \tag{2.22}$$

where $\lambda(LS)$ is the spin-orbit constant. The s.-o. interaction $\hat{\mathcal{H}}_{\mathrm{SO}}$ again lowers the degeneracy by splitting the terms into *multiplets* denoted by ${}^{2S+1}L_J$[9] where letters S, P, D, F, G, H, I are used instead of the numeric value of L. The ground state multiplets are determined by the rules formulated by Friedrich Hund stating that

- the term with maximum S has the lowest energy
- for a given S, the term with the largest L lies lowest in energy
- $J = |L+S|$ for more then half filled shells; $J = |L-S|$ for the less then half filled shells

The ground state multiplets of the R^{3+} ions as well as the g_J and the theoretical μ_{eff} values can be found in Tab. 2.1.

The crystal field Hamiltonian $\hat{\mathcal{H}}_{\mathrm{CF}}$ describes the effect of electrostatic field of the charges surrounding the rare-earth ion. The model is based on a simple coulombic interaction of the electrons with their neighbouring point charges, whose electric potential can be expanded into so-called tesseral harmonics and subsequently the evaluation of the matrix elements of the Hamiltonian can make use of the Stevens' operator equivalents [24] ${\hat{O}_n}^m$. The Hamiltonian can then be written as

[8] with spin

[9] both ${}^{2S+1}L$ and ${}^{2S+1}L_J$ are called term symbols

$$\hat{\mathcal{H}}_{\mathrm{CF}} = \sum_{n,m} {B_n}^m \hat{O}_n{}^m, \tag{2.23}$$

where ${B_n}^m$ are the crystal-field parameters, which can be either fitted from the experimental data or calculated ab initio. The crystal field adopts the symmetry of the lattice which often reduces the number of the parameters for cubic, tetragonal, etc. solids. The Stevens' operators $\hat{O}_n{}^m$ are a function of $\hat{J}_z$, $\hat{J}_+$, $\hat{J}_-$ and the squared magnitude of total momentum. For example

$$\begin{aligned} O_2{}^0 &= 3J_z^2 - J\left(J+1\right) \\ O_4{}^0 &= 35J_z^4 - 30J\left(J+1\right)J_z^2 + 25J_z^2 - 6J\left(J+1\right) + 3J^2\left(J+1\right)^2 \end{aligned} \tag{2.24}$$

The matrix elements of the operators are tabulated for all available values of J in rare earth multiplets or can be simply calculated from definition.

Itinerant Magnetism Model

In the absence of the magnetic field, the one-electron states with $s_z = \pm\frac{1}{2}$ are equivalent in terms of energy. The applied field B removes this degeneracy and splits the electrons into two sub-bands with $n_\uparrow$ and $n_\downarrow$ electrons. The magnetization is then given by

$$M = \mu_{\mathrm{B}}\left(n_\uparrow - n_\downarrow\right) = \mu_{\mathrm{B}}^2 B D(E_{\mathrm{F}}) = \frac{3N\mu_B^2 B}{2k_B T_F} \tag{2.25}$$

and the corresponding phenomenon, that is the positive susceptibility χ_{Pauli} of Fermi gas is called Pauli paramagnetism. $D(E_{\mathrm{F}})$ here denotes the density of states at the Fermi level and T_{F} is the Fermi temperature.

The ferromagnetism of metals such as Fe, Ni or Co can be explained by a condition for a spontaneous spin splitting of bands known as the Stoner criterion

$$UD(E_F) > 1 \tag{2.26}$$

U denotes the interaction energy. One can arrive at this requirement by taking into account the energetic balance of the splitting the sub-bands at the Fermi level by δE. The changes in the kinetic and potential energy of the system caused by the splitting are

$$\begin{aligned} \Delta E_k &= \frac{1}{2} D\left(E_F\right)\left(\delta E\right)^2 \\ \Delta E_p &= -\frac{1}{2} U\left(D\left(E_F\right)\delta E\right)^2 \end{aligned} \tag{2.27}$$

The overall change in energy is then

$$\Delta E = \frac{1}{2} D\left(E_F\right)\delta E^2\left(1 - UD\left(E_F\right)\right) \tag{2.28}$$

and the Stoner criterion gives out when the splitting is energetically favorable. Even if the criterion is not met, the energy balance causes an enhancement to the Pauli paramagnetism in the interacting electron gas

$$\chi = \frac{\chi_{\mathrm{Pauli}}}{1 - UD\left(E_F\right)}. \tag{2.29}$$

Landau gave a correction to the paramagnetism of free electron gas caused by a change of the character of motion of the electrons in magnetic field

$$\chi_{\text{Landau}} = -\frac{1}{3}\chi_{\text{Pauli}}. \tag{2.30}$$

This effect is known as Landau diamagnetism.

2.1.3 Exchange interactions

The exchange interaction, the main origin of the effective field and long-range magnetic order, is caused by the Pauli principle acting together with the Coulomb repulsion. The result for the simple system of the H_2 molecule was generalized by Heisenberg and can be, in the case of a lattice, written as a sum

$$\mathcal{H}_{\text{Heisenberg}} = -\sum_{i,j} J_{ij}\hat{\boldsymbol{S}}_i\hat{\boldsymbol{S}}_j \tag{2.31}$$

between atomic spins $\hat{\boldsymbol{S}}_i$ and $\hat{\boldsymbol{S}}_j$. J_{ij} is the exchange constant and has units of energy.

The $4f$ electrons of rare-earth ions in intermetallics are localized deep in the atomic shell, ie. without direct overlap, and interact via electrons in the 5d/6s conduction band. This mechanism is called RKKY interaction after Ruderman, Kittel, Kasuya and Yosida who showed the long-range oscillatory nature of this type of spin coupling. In the rare-earth ion group, only gadolinium has $S = J$. For the rest of the group it is needed to project S onto J first to be able to calculate the exchange coupling. This brings a factor

$$G = (g_J - 1)^2 J(J+1) \tag{2.32}$$

as $\boldsymbol{J} = \boldsymbol{L} + \boldsymbol{S}$ and $g_J\boldsymbol{J} = \boldsymbol{L} + 2\boldsymbol{S}$ and the Heisenberg hamiltonian is a square expression in $\boldsymbol{S}$. The effective coupling constant is then proportional to G and the magnetic ordering temperatures for series of rare-earth compounds with similar lattice spacings and conduction-band structure should scale with G, known as the de Gennes factor [25].

The other basic types of exchange interactions include the direct interaction in metals and the superexchange in insulators. Direct interaction involves overlapping d-orbitals in $3d$ metals and is short-range. The direct interaction can explain why half-filled bands such as in Cr and Mn tend to be anti-ferromagnetic while nearly-filled or nearly-empty bands are ferromagnetic as in iron [25]. In insulators, there is no direct $3d$-$3d$ orbital overlap but the interaction is mediated by the hybridized ligand orbitals sitting between the magnetic sites.

2.1.4 Types of magnetic ordering

From the phenomenological point of view, it has been observed that many materials go through a change of the nature of their magnetic properties - a phase transition - at a certain temperature when being cooled from the high-temperature[10] paramagnetic region. When the interactions between magnetic sites become

[10] or room-temperature

stronger than thermal fluctuations, the ordered state is energetically favorable and the magnetic order appears. In this paragraph I will give a short overview of the two basic types of magnetic ordering:

A ferromagnet has a non-zero spontaneous magnetization at temperatures $T < T_{\mathrm{C}}$, where T_{C} is its Curie temperature and all microscopic moments are, in the simpliest picture, pointing in the same direction. Ferromagnetism can be explained by a positive contribution of the Weiss molecular field $B_E = \lambda M$ and a self-consistent solution of Eq. 2.10 without external field. The influence of the molecular field leads to a shifting of the susceptibility in the paramagnetic region.

The antiferromagnets also exhibit a long-range order, as shown, for example, by new peaks on the neutron diffractogram, but the spontaneous magnetization does not appear. This case can, also in the simpliest picture, be perceived as presence of two ferromagnetic sublattices with moments pointing in opposite directions. The critical temperature T_{N} for an antiferromagnet is called the Néel temperature.

The behavior of the susceptibility of both ferromagnets and antiferromagnets can be described by the modified Curie-Weiss law

$$\chi = \frac{C}{T - \theta_{\mathrm{p}}} + \chi_0, \tag{2.33}$$

where χ_0 is the temperature-independent contribution to χ, C is a constant and θ_{p} is the Weiss temperature while $\theta_{\mathrm{p}} > 0$ for ferromagnets and $\theta_{\mathrm{p}} < 0$ for antiferromagnets.

2.2 X-ray diffraction on crystal structure

X-ray diffraction is one of the most basic and widely available tools in condensed matter physics and is regularly used to determine the details of the atomic structure of a studied compound. An ideal crystal is created by attaching a set of atoms identically to every lattice point $\boldsymbol{r}$, $\boldsymbol{r}'$ defined as

$$\boldsymbol{r}' = \boldsymbol{r} + u_1\boldsymbol{a}_1 + u_2\boldsymbol{a}_2 + u_3\boldsymbol{a}_3,\ u_i \in \mathbb{Z} \tag{2.34}$$

where $\boldsymbol{a}_i$ are linearly independent translation vectors. If all points that have the same surrounding arrangement of atoms are defined by Eq. (2.34), we have a primitive unit cell. Often it is convenient to define a bigger cell which has a simpler relation to the point symmetry of the structure. Such cell is called an elementary unit cell and can be centered, ie. it may contain more than one primitive lattice point. For the description of crystal planes, either diffraction indices or the so-called Miller indices (incommensurable), both using the (hkl) notation are used. Brackets are used to describe crystal directions, for example $H \,||\, [001]$ means magnetic field along the c-axis.

Using a simple idea of constructive interference of the x-rays on succesive crystallographic planes, one can arrive at the condition known as Bragg's law[11]

$$2d_{hkl} \sin\theta_{hkl} = \lambda, \tag{2.35}$$

[11] diffraction indices (hkl) used

where d_{hkl} is the inter-planar distance of the planes, $2\theta_{hkl}$ is the diffraction angle and λ is the wavelength of the incident x-ray beam.

The diffracted intensity I is proportional to the structure factor F_{hkl}

$$I \propto |F_{hkl}|^2 , \tag{2.36}$$

defined as

$$F_{hkl} = \sum_i f_i (\boldsymbol{q})\, e^{-i\boldsymbol{q}\boldsymbol{r}_i} e^{-W_i}, \tag{2.37}$$

where the sum goes over atoms in the unit cell. The atomic scattering factor $f_i(\boldsymbol{q})$ is defined as the Fourier transform of the charge density of a corresponding atom and is a function of the scattering vector $\boldsymbol{q}$. The last term in formula, the Debye-Waller (or B) factor accounts for the thermal vibrations of atoms in the unit cell.

2.3 Termodynamic properties

Heat capacity at constant pressure (volume) is defined as

$$C_{P,V} = T \left(\frac{\partial S}{\partial T} \right)_{p,V} , \tag{2.38}$$

where S denotes the entropy. The value of C_P can be measured rather easily - it is much easier to monitor the pressure in the sample chamber during experiment than to monitor changes in volume - whereas theoretical calculations are mostly operating with C_V because it does not incorporate the work done through expanding the volume of the sample. The relation [26]

$$C_P - C_V = VT \frac{\alpha^2}{\kappa_T} \tag{2.39}$$

holds. Here α denotes the thermal expansion coefficient and κ_T the isothermal compressibility. According to [26] the difference can be neglected at temperatures well below the room temperature, eg. for $T < 100\,\mathrm{K}$.

Phase transitions

According to the Ehrenfest classification, phase transitions are described by the lowest derivative of the Gibbs free energy

$$G\,(p,T) = U + pV - TS \tag{2.40}$$

that is discontinuous at the transition temperature. For the first-order transitions this means that a discontinuity in volume and entropy

$$\left(\frac{\partial G}{\partial T} \right) = -S, \left(\frac{\partial G}{\partial p} \right) = V, \tag{2.41}$$

are observed. The change in entropy is related to the latent ("hidden") heat absorbed or released during the transition.

Magnetic phase transitions are most often second-order transitions and bring a discontinuity in heat capacity

$$C_p = -T\left(\frac{\partial^2 G}{\partial T^2}\right)_p \tag{2.42}$$

while there is no discontinuity in S.

Specific heat, Magnetic Entropy

In the following sections, we will be relating thermodynamic quantities to one mole of a substance, ie. the definition in Eq. (2.38) will turn into a (molar) specific heat.

The specific heat is an additive quantity and can be written as a sum of contributions of phonons, conduction electrons (for conductive materials) and the magnetic contribution (when there is a magnetic phase transition or the Schottky contribution); the C_{etc} term stands for the aggregate value of other contributions[12]:

$$C = C_{\text{ph}} + C_{\text{e}} + C_{\text{mag}} + C_{\text{etc}} \tag{2.43}$$

The lattice vibrations (phonons) are responsible for both the high-temperature behavior of solids known as the Dulong-Petit law and the T^3 dependence observed at low temperatures. A solid with p atoms in a primitive cell will have 3 acustic phonon modes and $3p-3$ optical modes which differ in the $\omega(k)$ relation. The Einstein model describes well the optical modes as oscillators with a constant ω independent of the wave vector k. The characteristic parameter of this model is the Einstein temperature

$$\theta_E = \frac{h\omega}{k_{\text{B}}} \tag{2.44}$$

and the contribution to specific heat predicted within this model is

$$C_{\text{ph}}^{\text{Einstein}} = 3R\left(\frac{\theta_E}{T}\right)^2 \frac{e^{\theta_E/T}}{\left(e^{\theta_E/T}-1\right)^2}. \tag{2.45}$$

R denotes the gas constant. The Debye model which is suitable for description of the acustic phonons is based on the assumption of a linear dependence of ω on k and prescribes

$$C_{\text{ph}}^{\text{Debye}} = 9R\left(\frac{T}{\theta_D}\right)^3 \int_0^{\theta_D/T} \frac{x^4 e^x}{\left(e^x-1\right)^2}\mathrm{d}x, \tag{2.46}$$

where the parameter, the Debye temperature, is defined as

$$\theta_D = \frac{h\omega}{k_{\text{B}}}. \tag{2.47}$$

In materials which are conductive there will be an electron contribution to the total specific heat

$$C_{\text{el}} = \frac{1}{2}\pi^2 N_{\text{A}} k_{\text{B}} \frac{T}{E_{\text{F}}} = \gamma T. \tag{2.48}$$

[12] such as the nuclear hyperfine contribution.

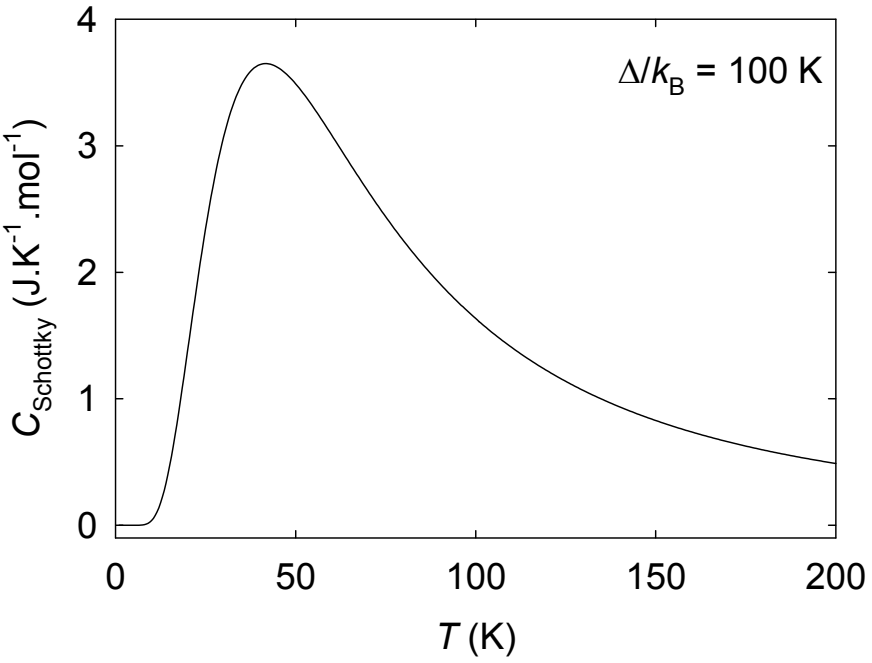

Figure 2.2: $C_{Schottky}$ for a two level system with $\frac{\Delta}{k_{\mathrm{B}}} = 100\,\mathrm{K}$ with the maximum at around 40 K.

This contribution is important mostly for temperatures below 5-10 K. The coefficient γ of the linear dependence is related to the effective electron mass of the conduction electrons and is known as the Sommerfeld coefficient.

For a system with energetic levels ε_i (in K) arising from the crystal field, the magnetic contribution to the total C is known as the Schottky specific heat

$$C_{\mathrm{Schottky}} = \frac{R}{T^2}\left(\sum \varepsilon_i^2 p_i - \left(\sum \varepsilon_i p_i\right)^2\right), \tag{2.49}$$

where

$$p_i = \frac{e^{-\varepsilon_i/T}}{Z},\ Z = \sum e^{-\varepsilon_i/T}. \tag{2.50}$$

An example of a Schottky specific heat for a system with two levels is schematically shown in Fig. 2.2.

At a sufficiently high temperature all $(2J+1)$ energy levels, on some of which is the degeneracy lifted by crystal field, will be equally populated, leading to the high-temperature magnetic entropy

$$S_{mag} = R\ln\left(2J+1\right), \tag{2.51}$$

while at the temperature of the phase transition T_{N} only two levels are usually considered which results in

$$S_{mag}\left(T_{\mathrm{N}}\right) \approx R\ln 2. \tag{2.52}$$

2.3.1 Magnetic specific heat below T_{N} (T_{C})

At temperatures below T_{N} (T_{C}), the main part of C_{mag} is caused by magnetic excitations or magnons. The basic textbook models [26] expect $C_{\mathrm{mag}} \propto T^n$ where

$n = 3$ for anti-ferromagnetics ($n = \frac{3}{2}$ for ferromagnetics). Due to magnetic anisotropy a gap in the magnon dispersion curve can emerge, introducing a factor $\exp\left(-\frac{\delta}{T}\right)$, where δ is the size of the gap [27]. The summarizing formula then looks

$$C_{\text{mag}} \propto T^{\frac{d}{m}} \mathrm{e}^{-\frac{\delta}{T}} \tag{2.53}$$

where d is the dimensionality of the excitation and $m = 1$ for an antiferromagnet (2 for ferromagnet).

3. Experimental and Computational Techniques Used

3.1 Crystal preparation

If we want to study the anisotropy of physical properties of a compound as a function of a (magnetic) field orientation to the main crystal axes, it is needed to grow the compound in the single-crystaline form. Otherwise one would get only an averaged value of the, for example, paramagnetic Curie temperature from a poly-crystalline sample. For properties which are not orientationally dependent such as the Neél temperature the use of a single crystal is not so important. The methods for crystal growing are essentially very simple in theory but rather demanding when it comes to the technical realization and the demands of the process such as ensuring the purity of the used elements or chemical inertness of the containers, atmosphere and tools. The temperature stability of the growth process is also a vital element of a sucessful growth. Apart from growth from vapour phase, the typology of single-crystal growth is divided between growth from solution (so called *flux*) and from melt which is usually used for congruently melting solids with no change of composition between the solid and liquid phase.

The mostly used methods for growth from melt are the *Bridgman method* where the growth is due to a temperature gradient in the melt, *zone melting* or the Czochralski process and similar crystal-pulling methods. The last two methods are widely used for industrial production of large ingots of silicon.

For the solution growth, a solvent with a relatively low melting temperature such as Ga (30 °C), In (157 °C), Sb (232 °C) or Al (660 °C). If the element used as a solvent is a part of the compound formula we speak of a *self-flux*. The solvent with the solute is heated up to a sufficiently high temperature and then slowly cooled allowing for creation of a saturated solution in which the single crystals grow. The cooling usually has to stop at some point and the crystals are decanted to prevent formation of an unwanted phase or phases which would emerge if the cooling continued to room temperature.

3.2 Sample Phase Analysis

The crystals obtained by growth from flux needed to be analysed for chemical composition and single crystal quality. The structural and phase analysis also needed to be done to ensure that the crystals represent well the studied compounds.

For our study we used the scanning electron microscope (SEM) equipped with an energy-dispersive X-ray spectrometry (EDX) probe.

3.2.1 SEM and EDX

Scanning electron microscopy uses a focused beam of electrons to obtain information about the topography and composition of a sample. The primary electrons with energies 10–100 keV hit the surface of a sample giving rise to the response

in form of secondary electrons, back-scattered electrons and characteristic X-ray radiation. The electron beam moves in the raster scan pattern which enables to obtain images that are visually similar to ones from the optical microscope. With SEM it is possible to achieve resolution up to few nm. The conventional SEM uses works with conductive samples which are put into a sample chamber and pumped to high vacuum. Any non-conductive part or for example piece of dirt on the sample surface would lead to accumulation of negative charge on it and subsequently to distortion of the image.

In the SE (secondary electrons) mode, the microscope detects low-energy electrons (< 50 eV) that were ejected from atoms in the sample by inelastic scattering. Depending on the angle between the normal to the sample surface and the electron beam, a different amount of the surface is irradiated resulting in different number of ejected secondary electrons. This makes the SE mode good for mapping the surface topography.

The BSE (back-scattered) electrons, on the other hand, are primary electrons that were deflected from the sample by a series of elastic collisions. Here the intensity is proportional to the local atomic number Z and the resultant image gives the qualitative information about 2D distribution of chemical composition.

The quantitative information about the composition can be obtained by analysing the characteristic X-ray spectra coming out of the sample, or the EDX (energy-dispersive X-ray analysis). These EDX spectra are generated when an electron hole is created in an inner shell of an atom by exciting the electron with the primary incident beam. An electron from a higher shell then jumps into this hole emitting the energy difference in form of an X-ray. The energy levels are characteristic for individual atoms so a spectrum can be fitted to obtain the elemental composition within an error of 1-2 %

3.3 X-ray scattering

Diffraction experiments were performed using the equipment of the Department of Condensed Matter Physics of Charles university in Prague.

Laue diffraction

For the analysis of a single-crystal and its orientation, the Laue method is widely used. It consists of irradiation of the sample by X-rays with a continuous 'white' spectrum. The diffraction maxima from either back-reflection or transmission geometry are collected on an image plate which is positioned perpendicularly to the incoming beam. For a given orientation, the Bragg condition is satisfied only for certain directions which will create a pattern that is visible on the image plate. Usually the method is used to orient the single crystal into one of its prominent crystal direction. In such case the Lauegram (the pattern collected via the Laue method) shows a symmetry which is directly relatable to the point group of the crystal. The presence of twinned points or circles would suggest that there are two crystals in the sample or that the sample is polycrystalline.

Powder diffraction

Powder diffraction (PDF) experiments on the samples obtained by single-crystal growth were performed using the conventional Bragg-Brentano $\theta - 2\theta$ geometry. Data were collected at room temperature using the Cu K_α spectral line and the obtained diffraction patterns were refined by Rietveld analysis using the Fullprof software suite [28].

3.4 Measurements of bulk physical properties

The magnetic and thermodynamical properties of studied samples were measured during experiments in the Joint Laboratory for Magnetic Studies, a joint facility of the Charles University (represented by the Department of Condensed Matter Physics) and the Institute of Physics of the Czech Academy of Sciences. The used equipment consisted of the Physical and Magnetic Property Measurement Systems (PPMS, MPMS) manufactured by Quantum Design). The PPMS is a versatile system for measuring heat capacity, magnetization or resistivity in the magnetic field range of 0 - 14(9) T and temperatures down to 1.8 K. Using the Helium 3 option lowers the minimal attainable temperature to 0.35 K.

3.4.1 Magnetization

Magnetization of samples was measured using the superconducting quantum interference device (SQUID) on MPMS or using one of the DC Extraction (ACMS) or Vibrating sample measurement (VSM) modules on PPMS. The latter two methods use the basic principle of inducing voltage in a coil by moving a magnetized sample while SQUID measures is based on the phenomenon of flux quantization and the use of Josephson junctions.

Internal field

In a regular experimental setup, the magnetization distribution in a sample produces a demagnetizing field which subtracts itself from the external applied field H_0. Practically, the correction

$$H = H_0 - DM \tag{3.1}$$

is used albeit mathematically it is valid only for few special sample shapes where a uniform field produces uniform sample magnetization. For example, the sphere has $D = \frac{1}{3}$ or for thin films we have $D = 1$ when the field is applied perpendicularly to the surface [25]. The demagnetization correction is important when D or/and M is large[1], otherwise it has hardly a noticeable effect on the measured curves.

Useful formulas

The measurement systems and user software by Quantum Design use CGS units instead of SI. Thus, the applied field is measured in *Oersteds* and the sample

[1] often at high fields

magnetic moment has *emu* units which can easily become a source of confusion. To transform the results to units used in the scientific community, it is useful to consider following relationships and formulas, based on the correspondence of 1 Oe to $\frac{10^3}{4\pi}\mathrm{Am}^{-1}$ (and to $B = 10^{-4}$ T in vacuum) and 1 emu to 10^{-3} Am^2, during numerical calculations.

$$\begin{aligned}
M\,[\frac{\mu_B}{f.u.}] &= m\,[\mathrm{emu}] \cdot \frac{1}{9,274 \cdot 10^{-21}} \cdot \left(\frac{m[\mathrm{mg}]}{m_{f.u.}[\mathrm{mg}]}\right)^{-1} \\
\chi\,[\frac{\mathrm{m}^3}{\mathrm{mol}}] &= M\,[\frac{\mu_B}{f.u.}] \cdot 5,585 \cdot \frac{4\pi \cdot 10^{-6}}{H\,[\mathrm{kOe}]} \\
M\,[\mathrm{Am}^{-1}] &= \frac{10^{-3} \cdot m\,[\mathrm{emu}]}{V\,[\mathrm{m}^3]} \\
H\,[\mathrm{Am}^{-1}] &= \frac{10^3}{4\pi} \cdot H\,[\mathrm{Oe}] \\
H\,[\mathrm{Oe}] &= \frac{4\pi}{10^3} \cdot H\,[\mathrm{Am}^{-1}] \\
H\,[\mathrm{Oe}] &= H_0\,[\mathrm{Oe}] - D \cdot \frac{4\pi}{10^6} \cdot \frac{m\,[\mathrm{emu}]}{V\,[\mathrm{m}^3]}
\end{aligned}$$

where $A\,[B]$ stands for value of quantity A in units of B. The $\frac{\mu_B}{f.u.}$ represents number of Bohr magnetons per formula unit. The numerical values used in formulas are directly related to values of μ_B and $N_A\mu_B$ while their use is justified by the measurement itself having a few orders of magnitude larger relative error.

3.4.2 Specific heat

The sample specific heat was measured using the relaxation method on PPMS 14 T. Apiezon N grease was used for good thermal contact of a sample with the platform on the puck. The PPMS first stabilizes the platform temperature, then applies power to the platform heater to achieve a certain temperature rise. The heater is then turned off and the temperature falls to its initial value. The changes in platform temperature are governed by simple differential equations. Depending on the quality of thermal contact between the sample and platform, a model with one or two relaxation coefficients has to be used.

3.5 Calculations

Octave [29] was used for calculations in this thesis. The used functions can be found in the last section of the thesis.

Octave is a free multi-platform interpreted programming and data manipulation language suitable for numerical calculations. It can be used interactively via a user interface just like an ordinary, yet advanced calculator or through writing user's own scripts and functions, while the built-in operators make matrix calculations easy. It can be used for solving various linear and nonlinear problems or for any thinkable numerical experiments. Octave allows double-precision[2] complex linear algebra. The language has a high degree of compatibility with MATLAB.

[2]approximately 16 decimal digits precision

	Y_2RhIn_8	La_2RhIn_8	Lu_2RhIn_8
γ ($mJ \cdot mol^{-1} \cdot K^{-2}$)	8.4	9.9	21.1
θ_D (K)	3×97	3×102	3×83
θ_{E_1} (K)	3×80	3×71	3×78
θ_{E_2} (K)	15×140	15×133	6×110
θ_{E_3} (K)	12×243	12×224	18×158
θ_{E_4} (K)			3×409
α (K^{-1})	1×10^{-4}	1×10^{-4}	1×10^{-4}

Table 3.1: Coefficients used for calculation of the specific heat of a non-magnetic analogue from Ref. [31]. The numbers of corresponding phonon branches are given before values.

3.5.1 Specific heat

The specific heat of La_2RhIn_8 that was used as a non-magnetic analogue to the studied compound Nd_2IrIn_8 was calculated using both Debye and Einstein models with a correction for anharmonicity [30] from values in [31] (shown in Tab. 3.1) as

$$C = C_\mathrm{e} + C_\mathrm{ph} = \gamma T + \frac{1}{1 - \alpha T}\left(3C_D\left(T, \theta_D\right) + \sum_{i=1}^{n} C_{Ei}\left(T, \theta_{E_i}\right)\right), \tag{3.2}$$

where α is the anharmonicity coefficient. n (and 3) here denotes the number of phonon branches.

The calculated curves for R_2RhIn_8, R =Y, La, Lu are shown in Fig. 3.3.

3.5.2 CEF susceptibility and Schottky specific heat

The crystal-field Hamiltonian for tetragonal symmetry is given by

$$\mathcal{H}_\mathrm{CEF} = {B_2}^0\hat{O_2}^0 + {B_4}^0\hat{O_4}^0 + {B_4}^4\hat{O_4}^4 + {B_6}^0\hat{O_6}^0 + {B_6}^4\hat{O_6}^4 \tag{3.3}$$

with Stevens operators $\hat{O_n}^m$ and corresponding CEF parameters ${B_n}^m$. The operators can be found in Tab. 3.2. Based on this model Hamiltonian, the theoretical susceptibility (for $H \to 0$) obtained by the second-order perturbation theory [17, 32, 33] is

$$\begin{aligned}\chi^i_\mathrm{CF} = N\frac{\left(g_J\mu_B\right)^2}{Z}\Bigg[&\frac{\sum_n \left|\left\langle n|\hat{J}_i|n\right\rangle\right|^2}{k_BT}\exp\left(-\frac{E_n}{k_BT}\right)\\ &+\sum_{n\neq m}\left|\left\langle m|\hat{J}_i|n\right\rangle\right|^2\frac{\exp\left(-\frac{E_n}{k_BT}\right)-\exp\left(-\frac{E_m}{k_BT}\right)}{E_m - E_n}\Bigg],\end{aligned} \tag{3.4}$$

where $i \in \{x, y, z\}$ is the direction of applied field and

$$Z = \sum_n \exp\left(-\frac{E_n}{k_BT}\right) \tag{3.5}$$

operator	
$\hat{O}_2{}^0$	$3\hat{J}_z^2 - J(J+1)$
$\hat{O}_4{}^0$	$35\hat{J}_z^4 - 30J(J+1)\hat{J}_z^2 + 25\hat{J}_z^2$ $-6J(J+1) + 3J^2(J+1)^2$
$\hat{O}_4{}^4$	$\frac{1}{2}\left[\hat{J}_+^4 + \hat{J}_-^4\right]$
$\hat{O}_6{}^0$	$231\hat{J}_z^6 - 315J(J+1)\hat{J}_z^4 + 735\hat{J}_z^4$ $+105J^2(J+1)^2\hat{J}_z^2 - 525J(J+1)\hat{J}_z^2 + 294\hat{J}_z^2$ $-5J^3(J+1)^3 + 40J^2(J+1)^2 - 60J(J+1)$
$\hat{O}_6{}^4$	$\frac{1}{4}\left[\left(11\hat{J}_z^2 - J(J+1) - 38\right)\left(\hat{J}_+^4 + \hat{J}_-^4\right)\right.$ $\left. + \left(\hat{J}_+^4 + \hat{J}_-^4\right)\left(11\hat{J}_z^2 - J(J+1) - 38\right)\right]$

Table 3.2: Operators

is the partition function. The equation (3.4) was used to compare measured data to calculated curves. The matrix elements of Stevens operators in the $|J, J_z\rangle$ basis are tabulated in [34] for all l,m and J. An example of the notation used there is in Tab. 3.3. With *Octave*, it is more convenient to construct the operators directly from definition (Tab. 3.2) from the $\hat{J}_z$, $\hat{J}_+$,$\hat{J}_-$ operators which can be calculated in a simple way. Examples of the matrices of Stevens operators for the Nd^{3+} ($J = \frac{9}{2}$) ion are shown in Figs. 3.1 and 3.2. in the $\left|\frac{9}{2}, \frac{9}{2}\right\rangle$,$\left|\frac{9}{2}, \frac{7}{2}\right\rangle$,...,$\left|\frac{9}{2}, -\frac{9}{2}\right\rangle$ basis.

Very often the measured susceptibility is fitted to

$$\chi^i = \frac{1}{\frac{1}{\chi^i_{CEF}} - \lambda_i} + \chi^i_0, \tag{3.6}$$

where λ_i denotes the molecular field coefficient for the relevant direction. In addition to this, if someone wanted to calculate an estimate of the magnetization on applied field, they would have to solve the equation

$$M_i = \frac{1}{Z}\sum_n \left|\left\langle n|\hat{J}_i|n\right\rangle\right| e^{-\frac{E_n}{k_B T}} \tag{3.7}$$

with the total Hamiltonian[3]

$$\hat{\mathcal{H}} = \hat{\mathcal{H}}_{CEF} - g_J\mu_B\hat{J}_i(H + \lambda_i M_i) \tag{3.8}$$

self-consistently [17].

[3]in CGS

	F	$\pm 1/2$	$\pm 3/2$	$\pm 5/2$	$\pm 7/2$	$\pm 9/2$
$\hat{O}_2{}^0$	6	-4	-3	-1	2	6
$\hat{O}_4{}^0$	84	18	3	-17	-22	18
$\hat{O}_6{}^0$	5040	-8	6	10	-11	3
	F	$\left\langle \frac{5}{2} \middle\| -\frac{3}{2} \right\rangle$	$\left\langle \frac{7}{2} \middle\| -\frac{1}{2} \right\rangle$	$\left\langle \frac{9}{2} \middle\| \frac{1}{2} \right\rangle$	-	-
$\hat{O}_4{}^4$	$12\sqrt{7}$	$5\sqrt{3}$	$5\sqrt{2}$	$3\sqrt{2}$	-	-
$\hat{O}_6{}^4$	$60\sqrt{7}$	$-16\sqrt{3}$	$6\sqrt{2}$	$30\sqrt{2}$	-	-

Table 3.3: Values of operators

$$\begin{pmatrix} 36 & 0 & 0 & 0 & 0 & 0 & 0 & 0 & 0 & 0 \\ 0 & 12 & 0 & 0 & 0 & 0 & 0 & 0 & 0 & 0 \\ 0 & 0 & -6 & 0 & 0 & 0 & 0 & 0 & 0 & 0 \\ 0 & 0 & 0 & -18 & 0 & 0 & 0 & 0 & 0 & 0 \\ 0 & 0 & 0 & 0 & -24 & 0 & 0 & 0 & 0 & 0 \\ 0 & 0 & 0 & 0 & 0 & -24 & 0 & 0 & 0 & 0 \\ 0 & 0 & 0 & 0 & 0 & 0 & -18 & 0 & 0 & 0 \\ 0 & 0 & 0 & 0 & 0 & 0 & 0 & -6 & 0 & 0 \\ 0 & 0 & 0 & 0 & 0 & 0 & 0 & 0 & 12 & 0 \\ 0 & 0 & 0 & 0 & 0 & 0 & 0 & 0 & 0 & 36 \end{pmatrix}$$

Figure 3.1: Diagonal $\hat{O}_2{}^0$ operator for a $J = \frac{9}{2}$ ion (Nd^{3+})

$$60\sqrt{7}\begin{pmatrix} 0 & 0 & 0 & 0 & 30\sqrt{2} & 0 & 0 & 0 & 0 & 0 \\ 0 & 0 & 0 & 0 & 0 & 6\sqrt{2} & 0 & 0 & 0 & 0 \\ 0 & 0 & 0 & 0 & 0 & 0 & -16\sqrt{3} & 0 & 0 & 0 \\ 0 & 0 & 0 & 0 & 0 & 0 & 0 & -16\sqrt{3} & 0 & 0 \\ 30\sqrt{2} & 0 & 0 & 0 & 0 & 0 & 0 & 0 & 6\sqrt{2} & 0 \\ 0 & 6\sqrt{2} & 0 & 0 & 0 & 0 & 0 & 0 & 0 & 30\sqrt{2} \\ 0 & 0 & -16\sqrt{3} & 0 & 0 & 0 & 0 & 0 & 0 & 0 \\ 0 & 0 & 0 & -16\sqrt{3} & 0 & 0 & 0 & 0 & 0 & 0 \\ 0 & 0 & 0 & 0 & 6\sqrt{2} & 0 & 0 & 0 & 0 & 0 \\ 0 & 0 & 0 & 0 & 0 & 30\sqrt{2} & 0 & 0 & 0 & 0 \end{pmatrix}$$

Figure 3.2: Non-diagonal $\hat{O}_6{}^4$ operator for a $J = \frac{9}{2}$ ion (Nd^{3+})

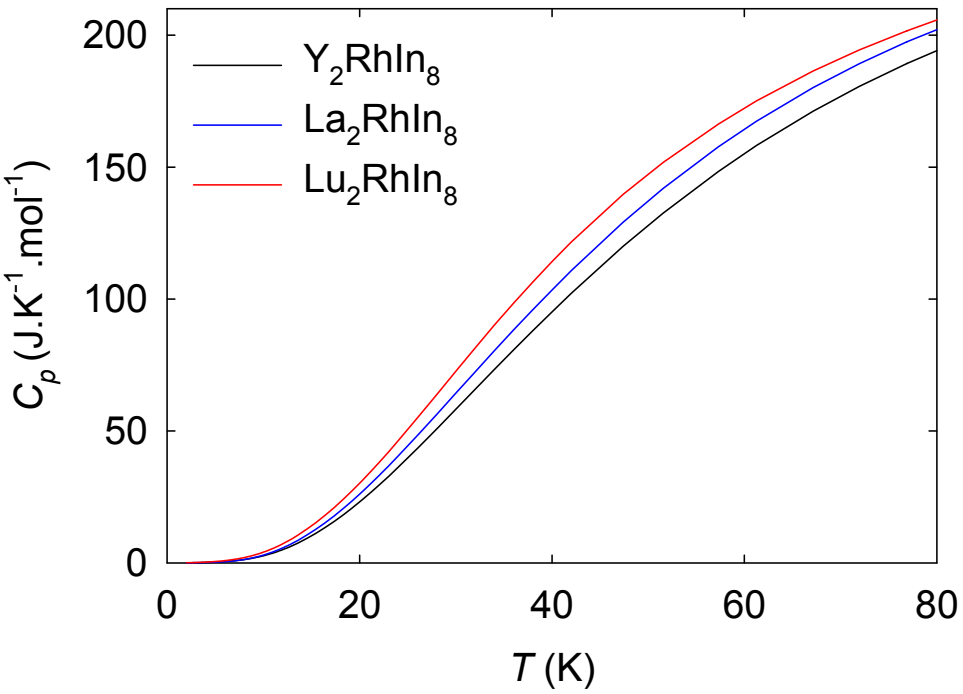

Figure 3.3: Specific heat of non-magnetic analogues in the relevant temperature region. La_2RhIn_8 was chosen as the closest non-magnetic analogue to Nd_2IrIn_8.

4. Results and Discussion

The results of the research done in the course of this thesis have been published in [35] and [36]. All data in the thesis was measured by the autor except for the specific heat of Nd_2IrIn_8 (measured by K. Vlášková).

4.1 Previous Results

Nd_2RhIn_8 and Nd_2IrIn_8 were previously studied by Pagliuso et al. [12] and Duque et al. [37] by means of magnetization and specific heat measurements. The Néel temperatures and polycrystalline average of μ_{eff} and θ_{P} obtained by Pagliuso et al. [12] are given in Tab. 4.1. Duque et al. [37] were able to derive a small part of the phase diagram for Nd_2RhIn_8 for field between 7 and 9 T which is shown in Fig. 4.1.

The physical properties of $R_mT_nX_{3m+2n}$ compounds have been systematically studied in [16, 17, 38] and a few complete phase diagrams are already known. As examples I show the phase diagrams of Dy_2CoGa_8, Dy_2RhIn_8 and $NdRhIn_5$ together with the measured curves, magnetization or specific heat, from which the diagrams were obtained in Figs. 4.2 and 4.3.

4.2 Crystal Growth

Single-crystalline samples of the studied compounds Nd_2RhIn_8 and Nd_2IrIn_8 were grown from an indium self-flux. High purity elements were used for the synthesis: 5N = 99.999% purity for In, 3N5 = 99.95% for the other elements. Multiple attempts with different starting stiochiometries ranging from 2:1:15 to 2:1:55 were needed to obtain satisfactory results. The temperature program consisted of a quick heating up to 1000 °C, 6h at the temperature for a proper homogenization of the solution, and slow cooling phase which reached 300 °C at a uniform rate of 3 °C/h. At 300 °C, the residual flux was removed using a centrifuge and the samples were collected. The same process and temperature program was used for both the Nd_2RhIn_8 and Nd_2IrIn_8 samples. Tab. 4.2 shows which starting compositions led to successful results.

The obtained crystals had the form of thin plates with thickness less than 0.5 mm and diameter of several mm. The weight of the resulting crystals was from 5 to 15 mg. Due to the shape of the single crystals, the data for $H||c$ were adjusted for a demagnetization factor estimated as $D = 0.9$.

	a (Å)	c (Å)	T_{N} (K)	μ_{eff} (μ_{B}/Nd^{3+})	θ_{p} (K)
Nd_2RhIn_8	4.640(3)	12.171(6)	10.7	3.57(3)	14
Nd_2IrIn_8	4.647(3)	12.139	12.3	3.60(3)	13

Table 4.1: Experimental parameters by Pagliuso et al. [12]

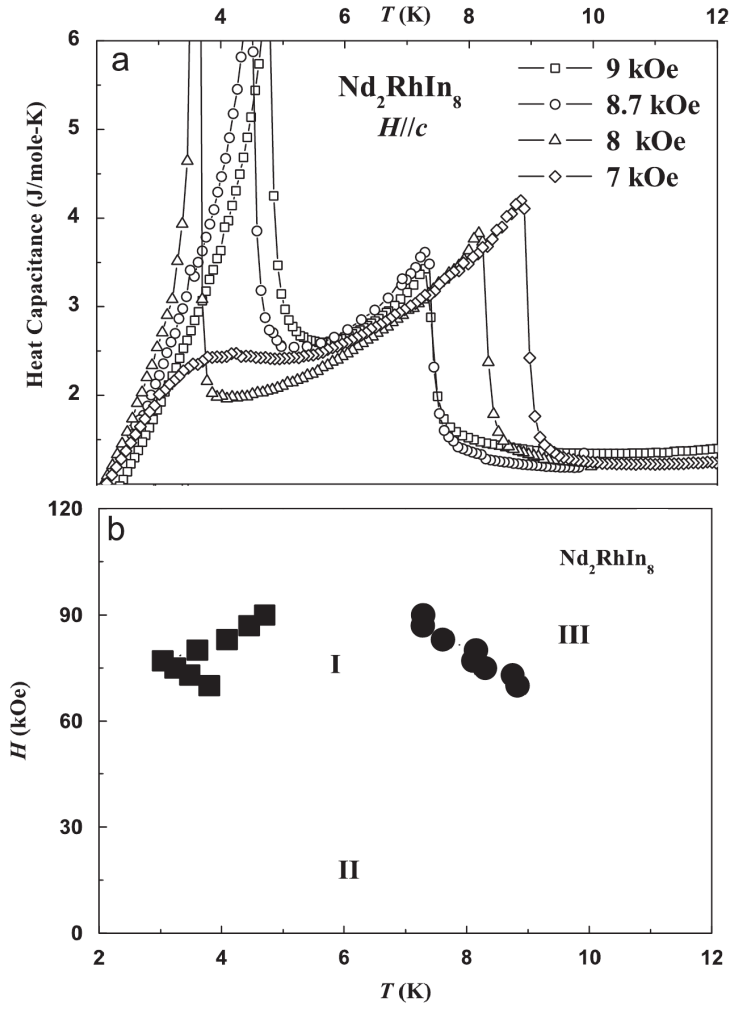

Figure 4.1: Phase diagram of Nd_2RhIn_8 by Duque et al. [37]

Compound	Starting stoichiometry	Result
Nd_2RhIn_8	2:1:25	Unsuccessfull
	2:1:40	Single crystals
	2:1:55	Unsuccessfull
Nd_2IrIn_8	2:1:15	Single crystals
	2:1:25	Unsuccessfull
	2:1:40	Unsuccessfull

Table 4.2: Results of the crystal growth as a function of the starting composition.

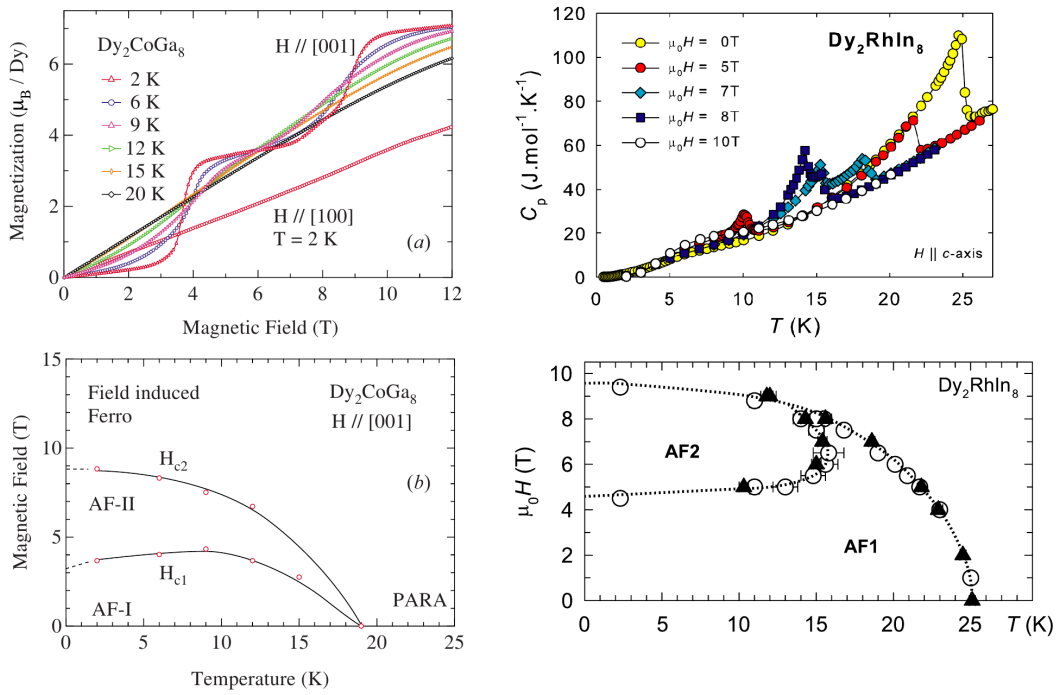

Figure 4.2: Phase diagrams of Dy_2CoGa_8 and Dy_2RhIn_8 and the curves used to determine the diagrams from Refs. [16] and [38]

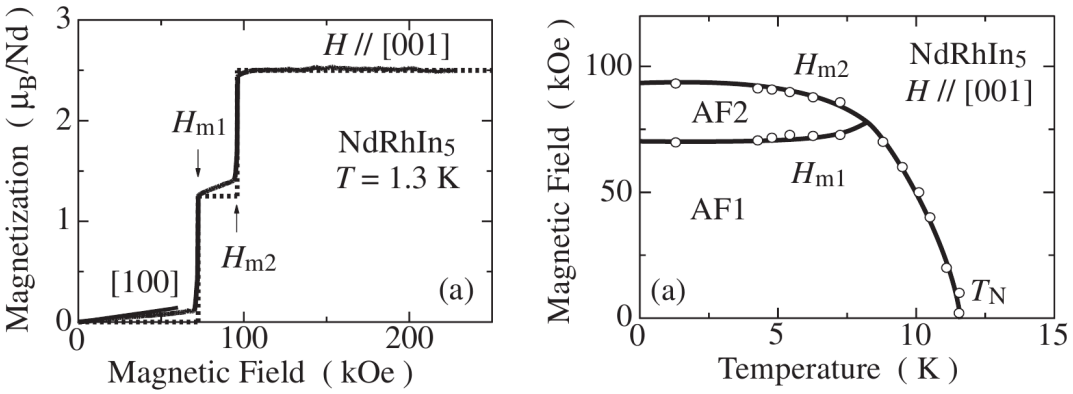

Figure 4.3: Phase diagram of $NdRhIn_5$ by Hieu et al. [17].

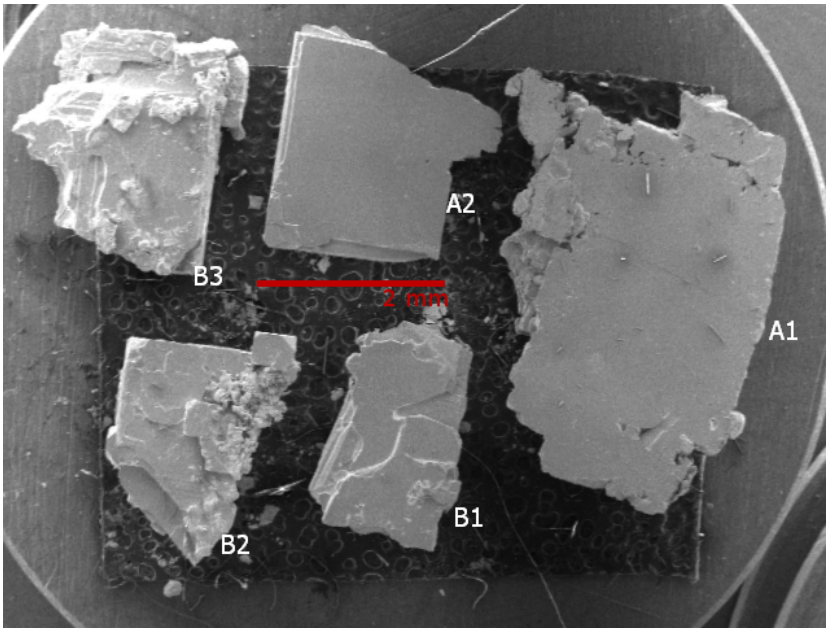

Figure 4.4: Nd_2IrIn_8 sample

	Nd_2RhIn_8	Nd_2IrIn_8	I. r. 2:1:8	I. r. 1:1:5	I. r. 1:3
R [at. %]	19.1(9)	17(1)	18.2 %	14.3 %	25 %
T [at. %]	8.9(8)	8(1)	9.1 %	14.3 %	0 %
X [at. %]	72(2)	75(3)	72.3 %	71.4 %	75 %

Table 4.3: Comparison of chemical compositions obtained by EDX to their ideal values. I. r. = Ideal (atomic) ratio.

4.3 Structure and Phase Analysis

The chemical composition was investigated by the energy-dispersive X-ray spectrometry (EDX) during scanning electron microprobe analysis. The surface of the crystals had to be polished before the EDX analysis.

A small amount of a Nd-In binaries $NdIn_{2.0(2)}$ and $NdIn_3$[1] was found on the crystal surface of the best Nd_2IrIn_8 sample that was used for measurements. The presence of a small amount (< 10 %) of a foreign phase could account for slight low-temperature anomalies in susceptibility and specific heat but its overall effect on phase diagrams determination is negligible.

Single crystals were oriented using the Laue method. The crystals of both compounds were thin plates with the *c*-axis perpendicular to the surface of the plate. Few single crystals from every batch were pulverized and analysed by X-ray powder diffraction. Apart from a single peak coming from the indium flux all peaks in the diffractogram could be described by the Ho_2CoGa_8 structure type of the compounds. The obtained unit cell parameters are shown in Tab. 4.5 compared to the other studies. Figs. 4.3, 4.3 and 4.3 show obtained Laue patterns, a simulated Laue pattern and the results of PDF on Nd_2IrIn_8.

[1]The existence of $NdIn_2$ has not yet been reported in literature.

Atom	Site symmetry	x	y	z
Nd	$2g$	0	0	z(Nd)
T	$1a$	0	0	0
In 1	$2e$	0	0.5	0.5
In 2	$2h$	0.5	0.5	z(In 2)
In 3	$4i$	0	0.5	z(In 3)

Table 4.4: Wyckoff positions in the unit cell. See Fig. 1.1 for the structure.

	Nd_2RhIn_8	Nd_2IrIn_8	Nd_2RhIn_8 [39]	Nd_2RhIn_8 [12]	Nd_2IrIn_8 [12]
a (A)	4.641(4)	4.650(3)	4.6213(9)	4.640(3)	4.647(3)
c (A)	12.167(6)	12.133(7)	12.113(3)	12.171(6)	12.139(6)
z(Nd)	0.308(2)	0.309(3)	0.3083(3)	-	-
z(In 2)	0.306(4)	0.309(3)	0.3059(6)	-	-
z(In 3)	0.120(2)	0.120(2)	0.1212(4)	-	-

Table 4.5: Comparison of measured structural parameters to studies by Čermák et al. [39] and Pagliuso et al. [12]. Data Ref. [39] were measured at $T = 2\,\mathrm{K}$ on the same single crystal as was used in this work. See Tab. 4.4 for the atomic positions inside the unit cell.

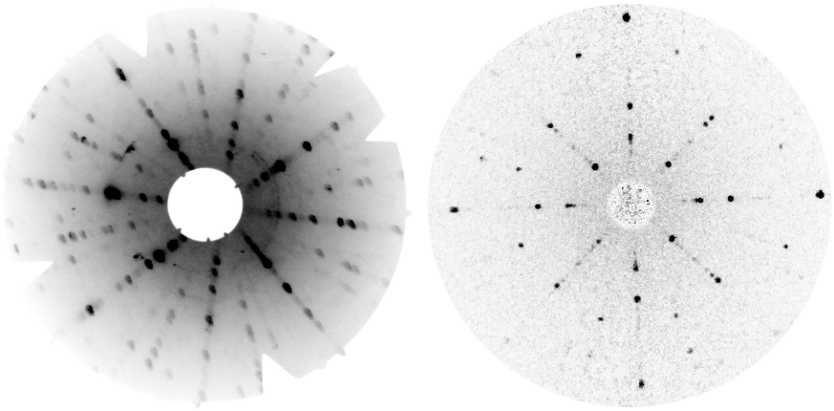

Figure 4.5: Laue patterns (inverted color) of crystals oriented with the plate surface perpendicular to the X-ray source. The four-fold symmetry and mirror planes are visible. The image on the left (right) is from the Nd_2RhIn_8 (Nd_2IrIn_8) sample. On the right, the c-axis of the crystal was precisely along the beam whereas on the left the crystal was slightly tilted.

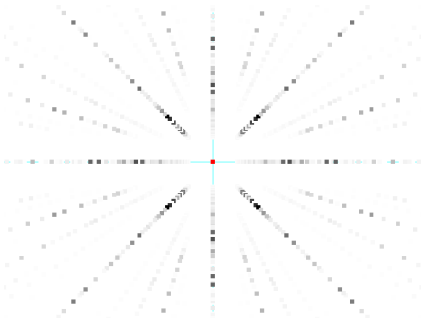

Figure 4.6: Software generated Laue pattern ("*LauePt*" suite used).

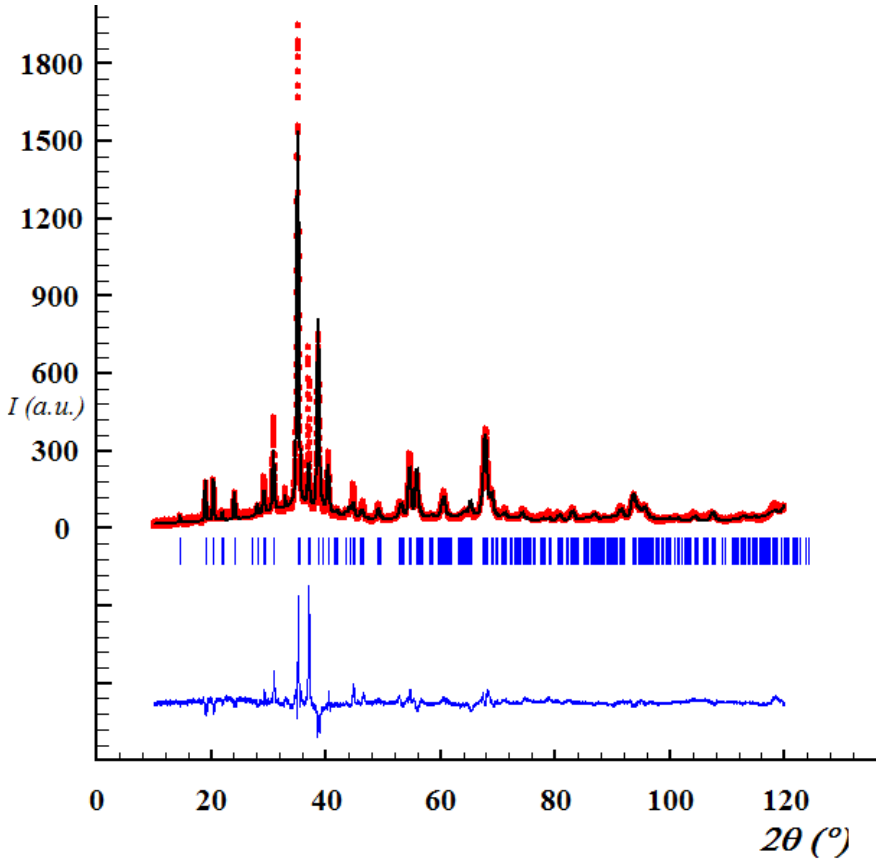

Figure 4.7: Rietveld refinement of the powder diffraction pattern on Nd_2IrIn_8 crystals. The difference around 40 ° is caused by a significant texture in the sample.

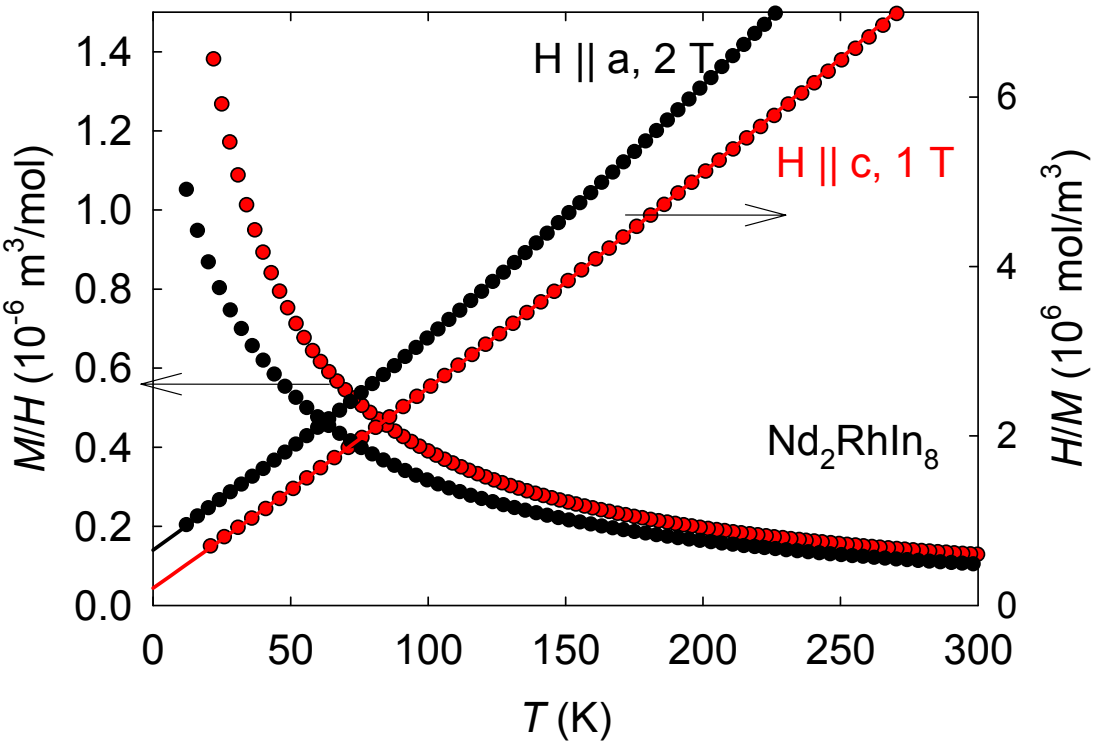

Figure 4.8: Susceptibility in the paramagnetic region. Parameters of the used fits are $\mu_{\text{eff}}^{c} = 3.75$, $\theta_{\text{p}}^{c} = -9.04\,\text{K}$, $\chi_0^{c} = -0.0156\,\frac{cm^3}{mol}$ for c, and $\mu_{\text{eff}}^{a} = 3.758$, $\theta_{\text{p}}^{a} = -28.3659\,\text{K}$, $\chi_0^{a} = -0.03135\,\frac{cm^3}{mol}$ for a.

4.4 Measurements and results discussion

4.4.1 Nd_2RhIn_8

Curie-Weiss law and low temperature susceptibility

As the first step, the susceptibility curves were measured for field directions H along a and c. Measured values are presented in Fig. 4.8. The inverse susceptibility curves were fitted to the Curie-Weiss law. The fit yields -28(2) K and -9(1) K for the a- and c-axis. The value of the effective magnetic moments 3.75(5) was obtained. The curvature of the dependencies needed to use the χ_0 at -0.031(5) and -0.016(4) respectively. The relatively high diamagnetic contribution χ_0 for the a direction which resulted from the fit causes the reciprocal susceptibility curve to be bent upwards in higher temperatures and could be caused by a diamagnetic impurity in the sample or by an effect during the measurement such as sample holder or the glue used.

The Neel temperature $T_{\text{N}} = 10.8(2)$K was derived from the low temperature susceptibility curves, which are displayed in Fig. 4.9. No difference was measured between zero-field cooled and field cooled curves. Contrary to the basic theory of antiferromagnetics, the susceptibility in the ordered moments' direction does not go to zero. Instead, an upturn at temperatures below 4 K is observed without a satisfactory explanation, as the high quality of the sample minimized the

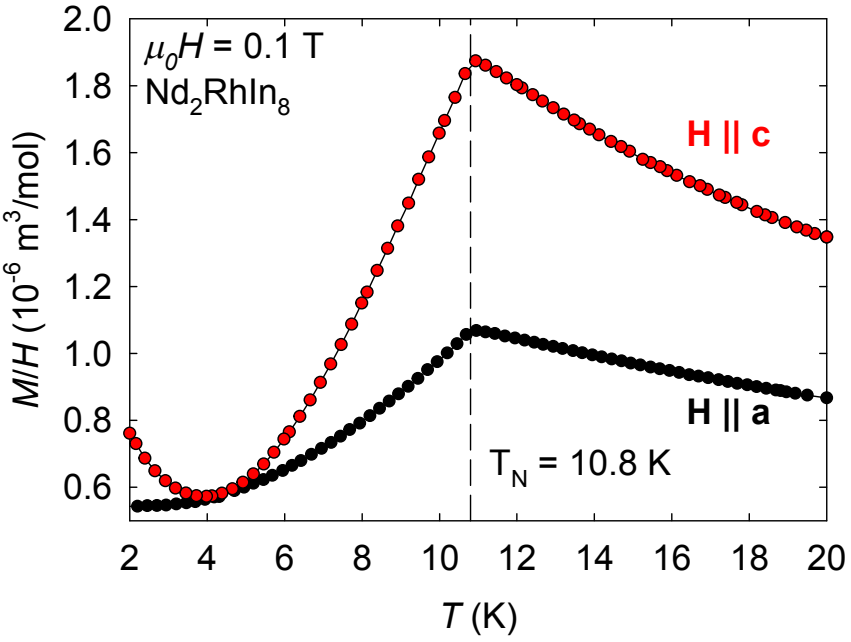

Figure 4.9: Low temperature susceptibility.

possibility of higher amount of impurities present and there is no other evidence which would indicate an additional phase transition in this temperature and field region.

Magnetization and construction of phase diagram

Multiple magnetization curves were measured both below and above the Néel temperature T_N. At 2 K, the curve has two sharp steps that are an indication of a transition into another magnetic phase. At higher temperatures a gradual change of shape and blurring of the steps is observed. The evolution of the magnetization is shown in Fig 4.10 and the comparison of the two main directions in Fig. 4.11.

Numerical derivative of the measured data was used to determine the phase diagram of the compound. Due to a large amount of noise, the measured curves had to be smoothed (and interpolated) with cubic splines before calculation of the derivative. The curves are displayed in Figs 4.12 and 4.13 together with their derivatives. For temperatures up to 5 K, two peaks are visible on the derivative. At 5.5 K the peaks had merged and it is possible to deduce only one transition temperature. The data were used to obtain the phase diagram of Nd_2RhIn_8 which can be found in Fig. 4.14. The phase diagram consists of two phases and bears clear similarity to phase diagrams of other members of the compound family. In comparison with [37] as shown in the figure, our measurements did not confirm an additional phase transition in the region $\mu_0 H < 8\,\mathrm{T}$ which is probably caused by a misinterpretation of broad anomalies in C_p as seen in Fig. 4.1 for $H = 7\,\mathrm{kOe}$. Continuing, we were not able to reproduce the exact border between phase I and II. This can have many causes ([37] does not offer error bars), but, taking into consideration that we have larger error in determination of transition field and [37] have error in deriving the transition temperature we believe that the phase

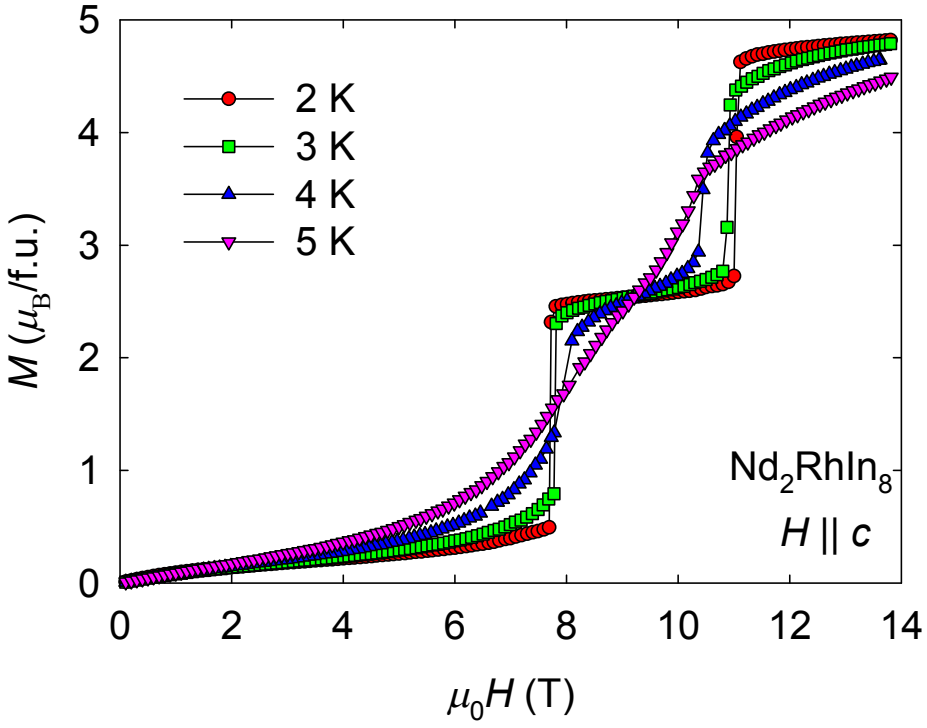

Figure 4.10: $M(H)$ curves with field along c.

border goes somewhere between the sets of points, as shown with the line in the Fig. 4.14. There was no indication in the measured date for existence of another phase between phases I and II.

The single crystal of Nd_2RhIn_8 prepared during this work was later used by Petr Čermak in his study of magnetic structures of R_2RhIn_8 (R = Nd, Dy and Er) [39] which revealed the magnetic propagation vector $k = \left(\frac{1}{2}, \frac{1}{2}, \frac{1}{2}\right)$ in Nd_2RhIn_8 and moments ordering along the c axis at temperatures below T_N which is in agreement with the compound's easy axis. The result of his work is shown in Fig. 4.15. Similarly, we also present the high-field magnetization data obtained by Prof. A.V. Andreev on our Nd_2RhIn_8 sample as an inset to Fig. 4.11. This inset can explain why at 2 K and 14 T, the observed moment ($\approx 2.5\,\frac{\mu_B}{Nd^{3+}}$) is significantly lower than the theoretical value of the saturated moment Eq. () 3.27 μ_B, that is the saturation sets in at even higher fields.

4.4.2 Nd_2IrIn_8

Susceptibility, Curie-Weiss law and CF susceptibility

The measured dependencies of the magnetization on temperature of Nd_2IrIn_8 single crystal are shown in Fig. 4.17. The H/M curves are linear in the paramagnetic region and exhibit Curie-Weiss behavior with a small deviation for H along c at high temperatures. The data indicate a transition to the antiferromagnetic state at $T_N = 12.5(2)$K (temperature obtained from specific-heat data, as indicated in next section) in good agreement with Ref. [12]. We observe a minimum of the magnetization and an increase below 6 K which might be attributed

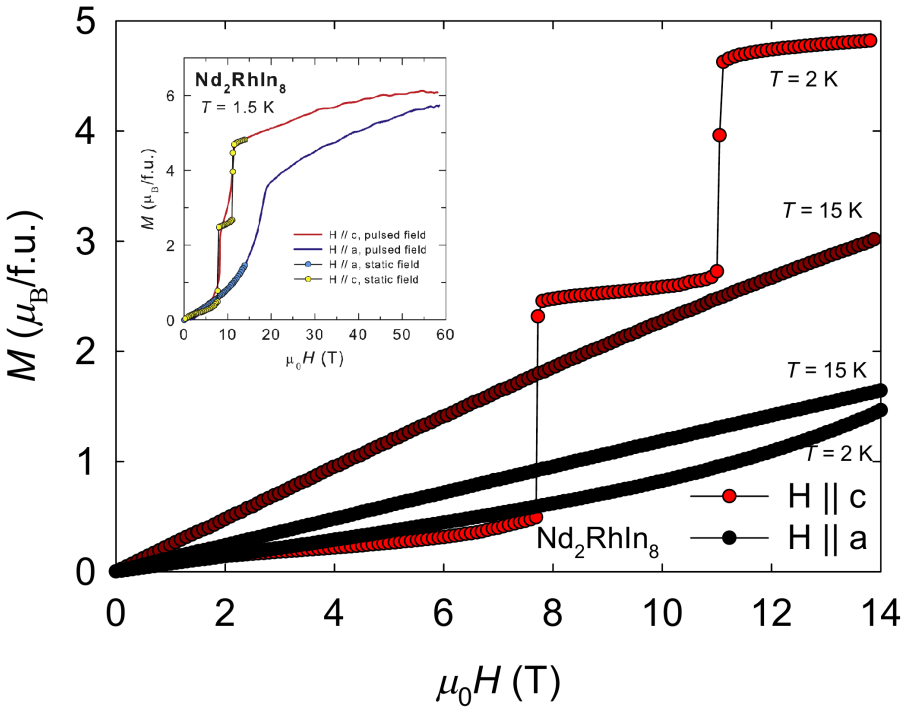

Figure 4.11: Comparison of magnetization curves for the a and c directions at temperatures below and above the Néel temperature T_{N}. The inset shows the high-field magnetization measured by Prof. Andreev [36] where it is possible to see the continuation of the bend on the $H||a$ curve at 2 K.

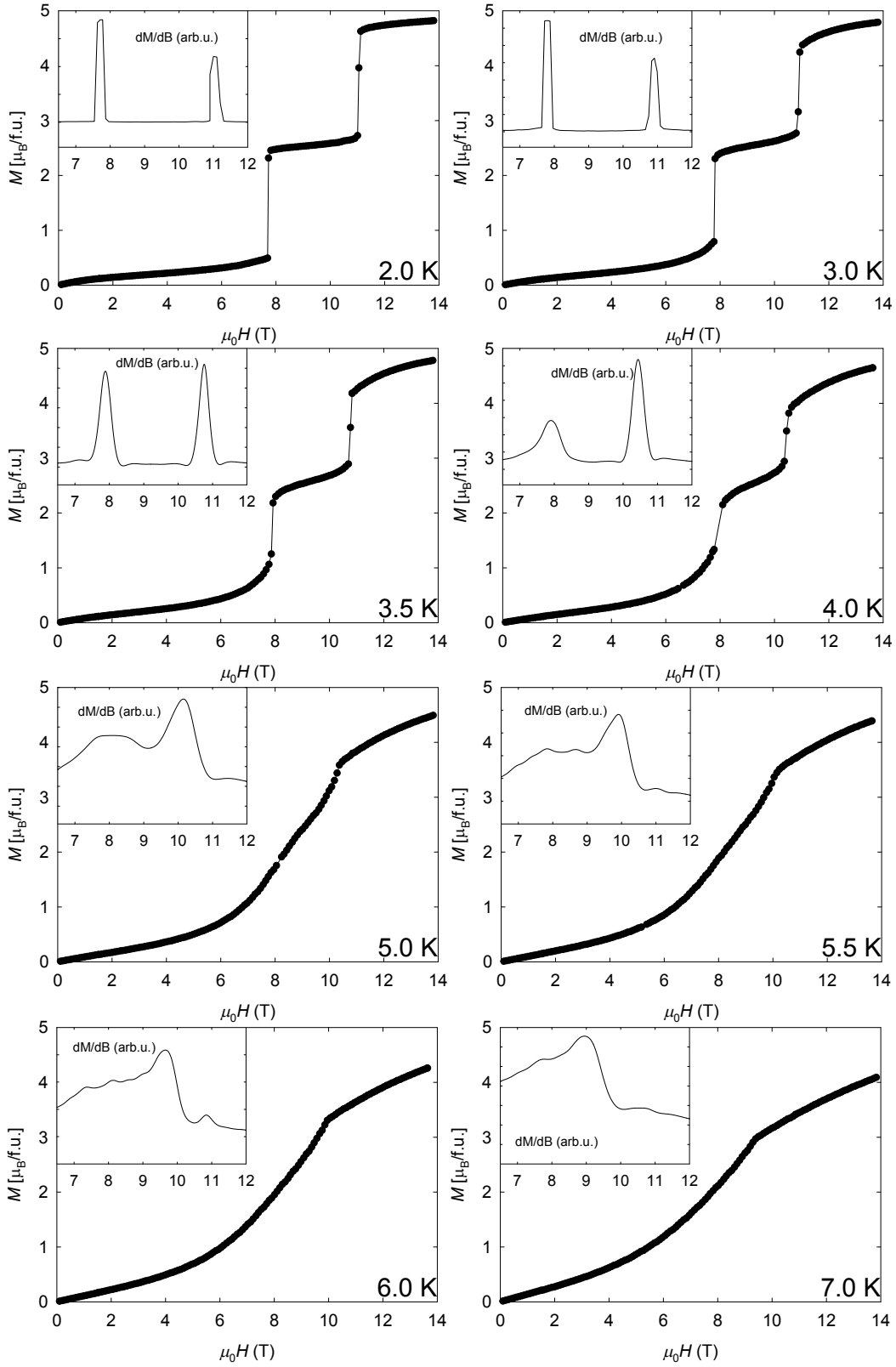

Figure 4.12: Nd_2RhIn_8 magnetization curves (part 1) with derivatives (ordered state) for $T = 2.0$ K to 7.0 K. Two transitions are visible at low temperatures and become blurred at higher temperatures.

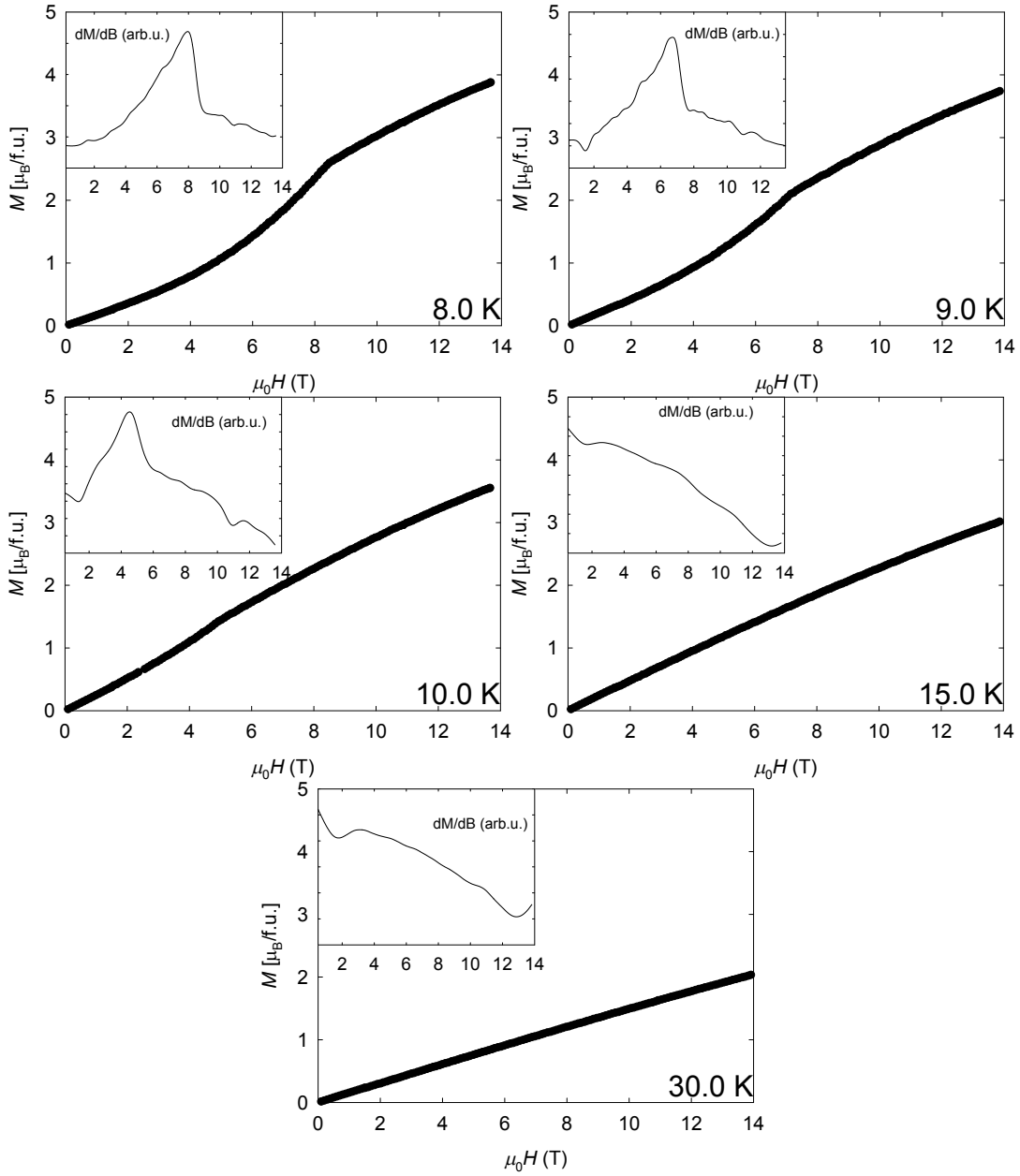

Figure 4.13: Nd_2IrIn_8 magnetization curves (part 2) with derivatives (ordered state) for $T = 8$ K, 9 K, 10 K, 15 K and 30 K. It is possible to detect one transition at $T < T_N$.

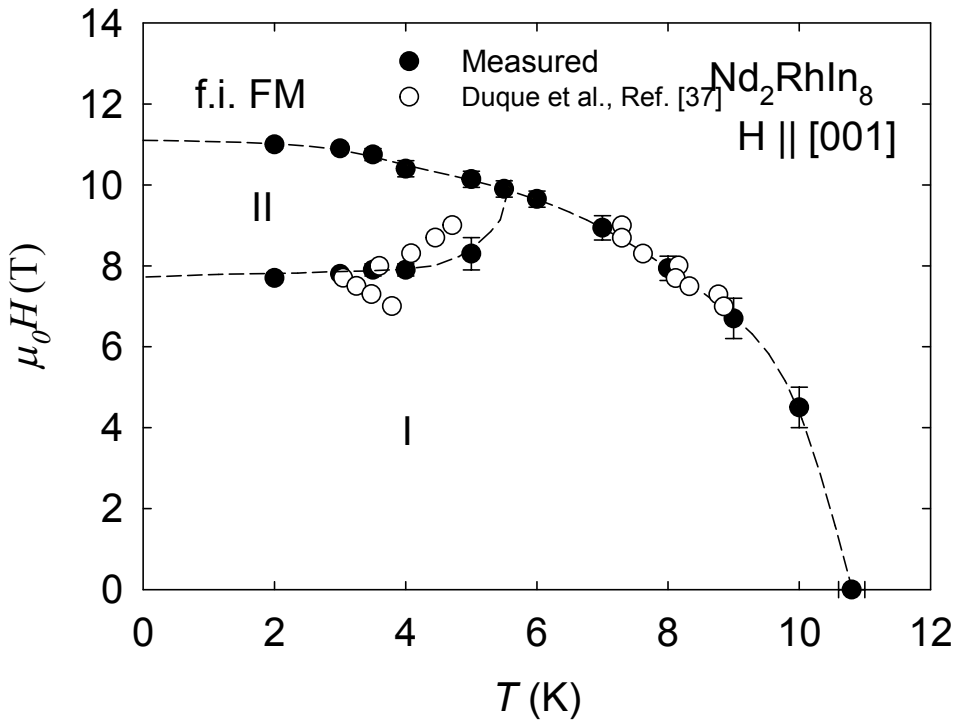

Figure 4.14: Nd_2RhIn_8 phase diagram for H along c.

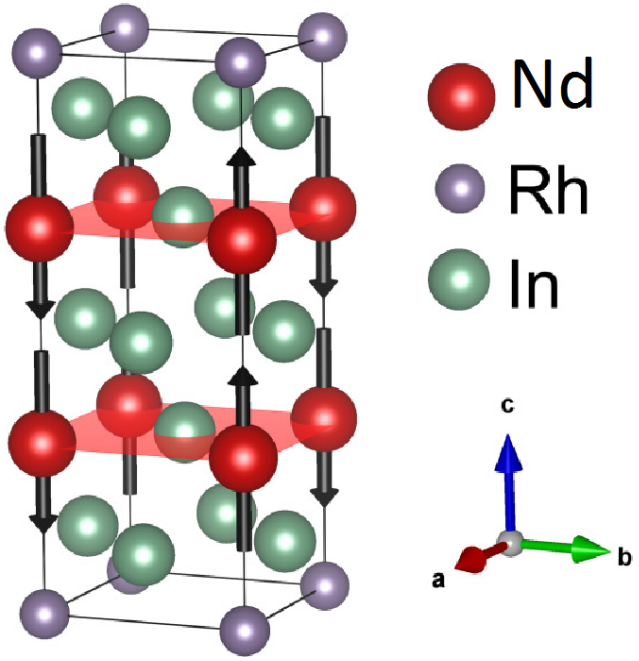

Figure 4.15: Magnetic structure of the I phase in Nd_2RhIn_8 obtained by Petr Čermák [39].

parameter	B_2^0	B_4^0	B_4^4	B_6^0	B_6^4
value (10^{-3} K)	-19.93	-2.89	-3.06	-0.304	10.25

Table 4.6: CF parameters from ab initio calculations.

to the presence of traces of $NdIn_3$ which orders magnetically just below 6 K [11]. The inverse susceptibility curves were fitted to the Curie-Weiss law which gives θ_p = -23(4) K and 4(4) K for the a- and c-axis, respectively. The effective magnetic moment per Nd^{3+} ion $\mu_{eff} = 3.61(8)\mu_B$ is in agreement with the theoretical free-ion value of 3.62 μ_B/Nd^{3+} ion. If the temperature independent χ_0 was fitted, it acquired values of 0.000(3) and -0.010(2) for the a and c directions, with a neglligible change in θ_p (within the error bars).

For the calculations on Nd_2IrIn_8, I used CF parameters obtained by Doc. Diviš from the first-principles calculation using the full potential augmented plane waves plus local orbitals (APW+lo) method [40, 41]. The CF parameters then originated from the aspherical part of the (total) single-particle potential.

The susceptibility calculated from the CF parameters (see Tab. 4.6) predicts c as the easy-axis. This is in agreement with the measurement yet the calculated curves exhibit only a minimal anisotropy between the a and c directions in comparison to the measured H/M curves (Fig. 4.18). This discrepancy is probably due to anisotropy of the molecular field acting on the Nd^{3+} ions.

Magnetization curves, $M(T)$ curves, phase diagram

The $M(H)$ curves are presented in Figs. 4.19 and 4.20. Two transitions are clearly visible at 2 K when the field is applied along the c-axis. Figure 4.19 shows the evolution of the metamagnetic transitions in a temperature range of 2 – 10 K. The transitions gradually blur and merge at about 6 K. Comparison of the magnetization curves measured for the magnetic field oriented along the c-axis and perpendicular to it, both in the ordered and the paramagnetic state, is presented in Fig. 4.20. The magnetic moment per one ion at 2 K and 14 T is again lower than the theoretical value but we believe this can be explained in a similar way as in Nd_2RhIn_8, that is the moments need more than 14 T to be fully saturated.

The magnetization was measured also as a function of temperature in magnetic fields up to 14 T. Representative data are shown in Fig. 4.21 for several values of the magnetic field. The individual curves are discussed below in connection with the magnetic phase diagram.

The measured $M(H)$ and $M(T)$ curves have been used to construct the magnetic phase diagram (Fig. 4.22) for $H||c$. The phase diagram is divided into two magnetic phases and has the same structure as has been reported for other R_2IrIn_8 compounds in which the magnetic moments are aligned along the c-axis [16, 39]. All parts of this phase diagram are well reflected in the $M(T)$ dependencies shown in Fig. 4.21. In fields below 7 T, only a magnetic transition from the paramagnetic to the antiferromagnetic phase I is seen. The data measured at 7.5 T and 8 T show the same transition to phase I as in lower fields but, in addition, the transition from phase I to phase II is reflected by a sharp increase of M. At 11 T, only the transition to phase-II is observed and the 12 T data show behavior of a field-induced ferromagnetic order. In analogy to recently studied

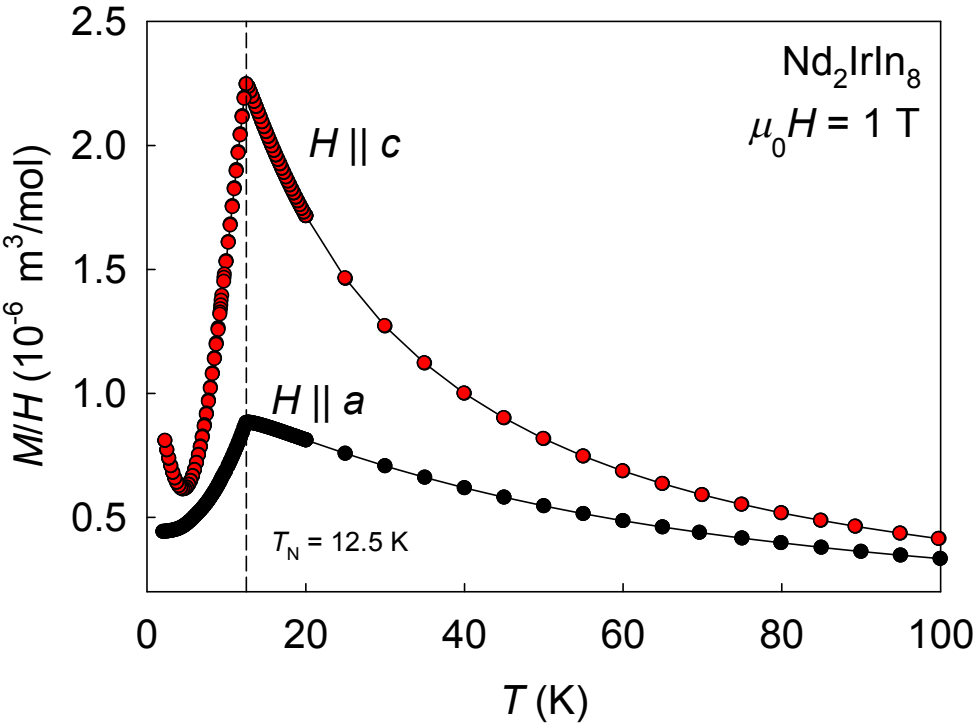

Figure 4.16: Low temperature detail of the measured M/H curve in c and a directions. (Compound: Nd_2IrIn_8).

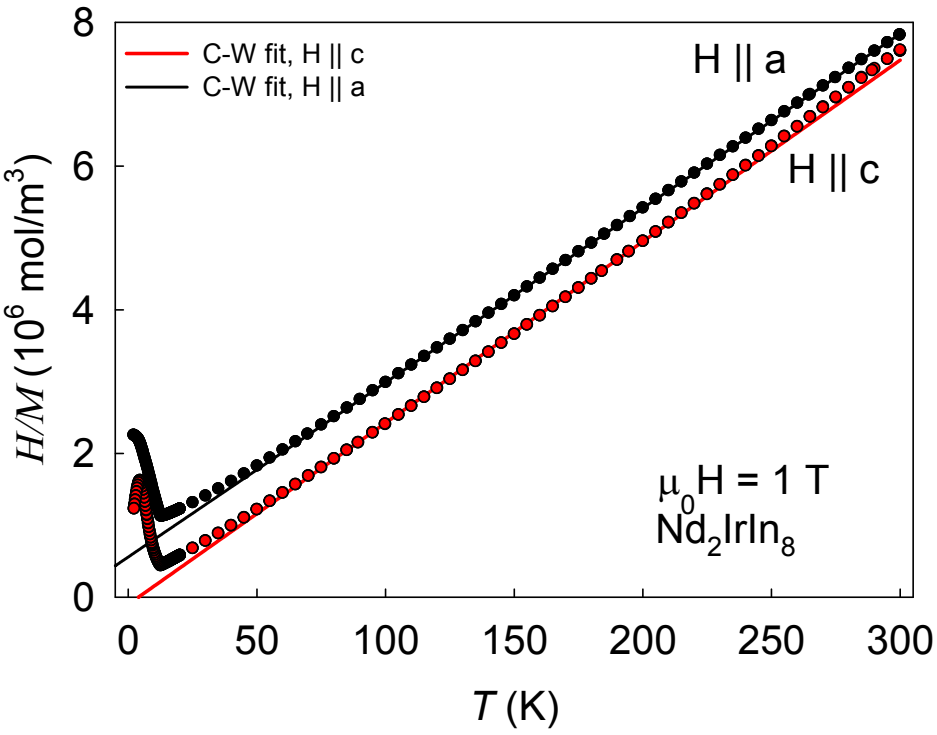

Figure 4.17: Measured H/M curves of Nd_2IrIn_8 for c and a directions fitted to the Curie-Weiss law. Parameters of fits used are $\mu_{\mathrm{eff}}^{c} = 3.55$, $\theta_{\mathrm{p}}^{c} = 4.0\,\mathrm{K}$ for c and $\mu_{\mathrm{eff}}^{a} = 3.62$, $\theta_{\mathrm{p}}^{c} = -23.02\,\mathrm{K}$ for a.

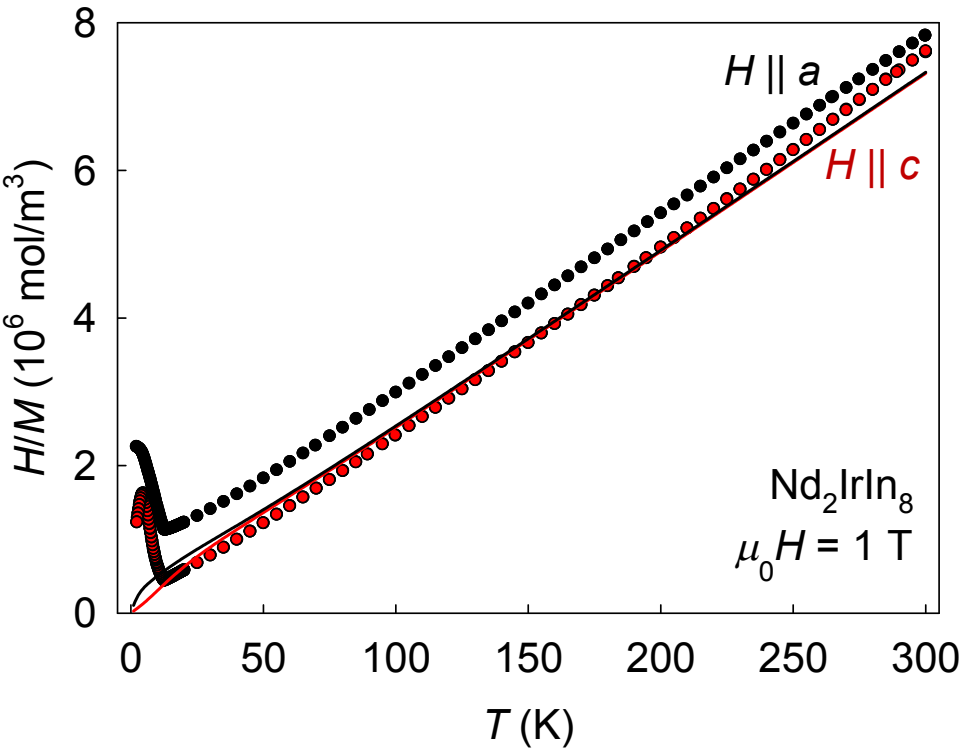

Figure 4.18: Comparison of the measured H/M curves of Nd_2IrIn_8 to the inverse susceptibility calculated from parameters in Tab. 4.6 by using .

Ho_2RhIn_8 [33] it is probable that in phase-II, half of the Nd moment value probably orders ferromagnetically. The magnetic structure of phase II in Ho_2RhIn_8 has been studied by neutron diffraction and revealed a non-trivial multi-k magnetic structure described by four propagation vectors including a ferromagnetic component $k = (0, 0, 0)$. The transition between phases I and II can be seen also as the flipping of a quarter of the magnetic moments which causes the total magnetization to be half of the field-induced ferromagnetic state value. Due to the similarities in the shape of the phase diagrams and the magnetization curves, it is possible to presume an analogous mechanism to be present in Nd_2IrIn_8.

Specific heat analysis

As the last step, the heat capacity of Nd_2IrIn_8 was analyzed. The $C_p(T)$ curve was used to determine the value of T_N. The low-temperature part of $C_p(T)$ is presented in Fig. 4.27. La_2RhIn_8 (data from Ref. [31], see Fig. 3.3) was used as the closest available non-magnetic analogue to enable us to calculate the magnetic heat capacity, the magnetic entropy and to estimate the Schottky specific heat above T_N. From Fig. 4.27 can be seen that only the R=La analogue has an acceptable entropy at higher temperature limit.

In the temperature range below T_N, the phonon contribution is rather small and the uncertainty introduced by the different masses of Ir and Rh is acceptably low. C_{mag} follows approximately the T^3 dependency expected for 3D antiferromagnetic magnons below T_N, except for the region below 6 K where it deviates

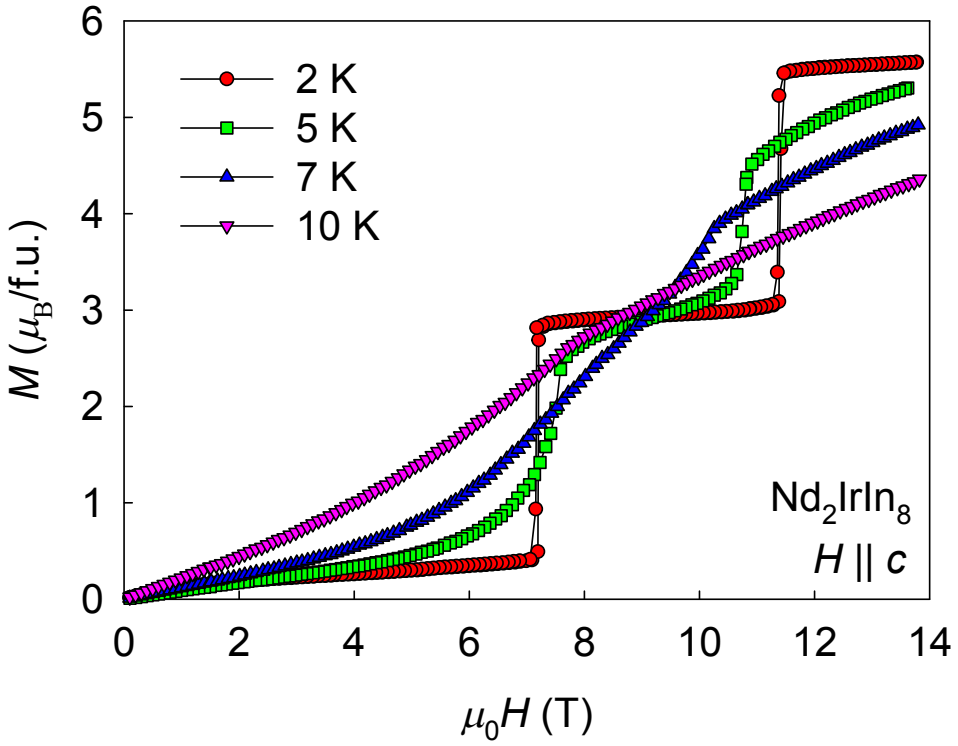

Figure 4.19: Nd_2IrIn_8 magnetization curves for H along c. Evolution of the transitions in temperatures up to 10 K.

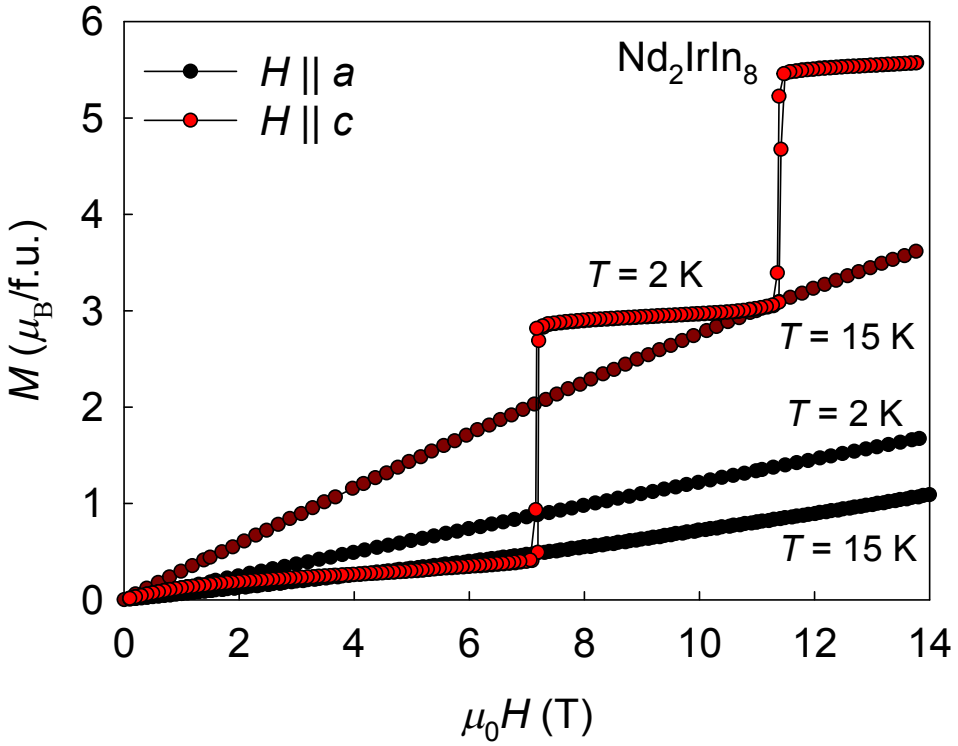

Figure 4.20: Comparison of magnetization curves above and below T_N for H along both c and a.

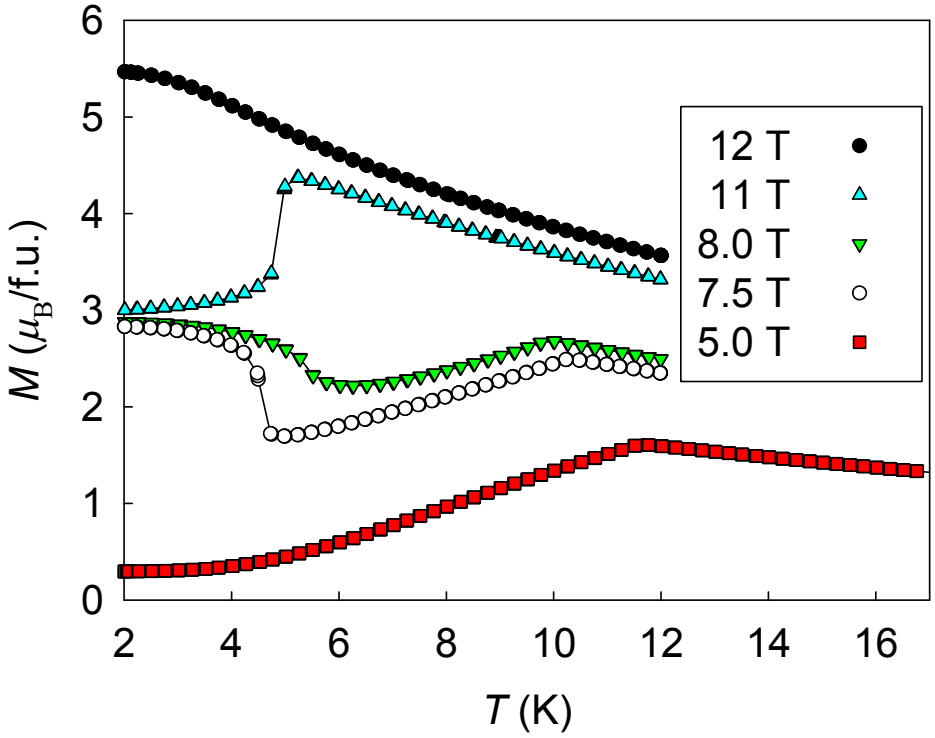

Figure 4.21: Comparison of selected $M(T)$ curves at $\mu_0 H = 5$ to 12 T. The transition into the second phase is observed at fields 7.5 T, 8 T and 11 T.

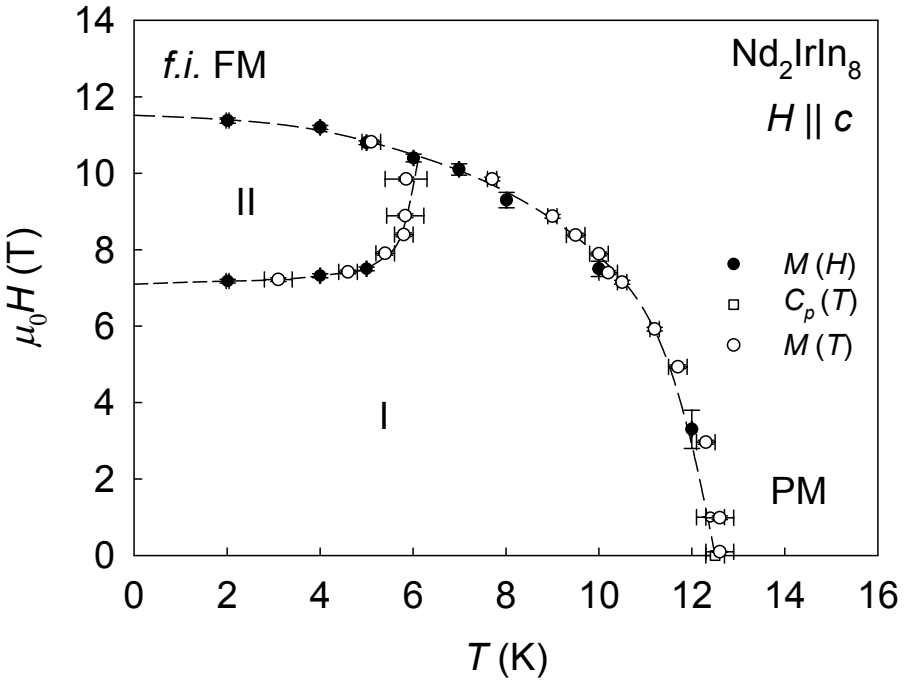

Figure 4.22:]
The magnetic phase diagram of Nd_2IrIn_8 obtained from magnetization curves $M(H)$ and $M(T)$ and specific heat $C_p(H)$.

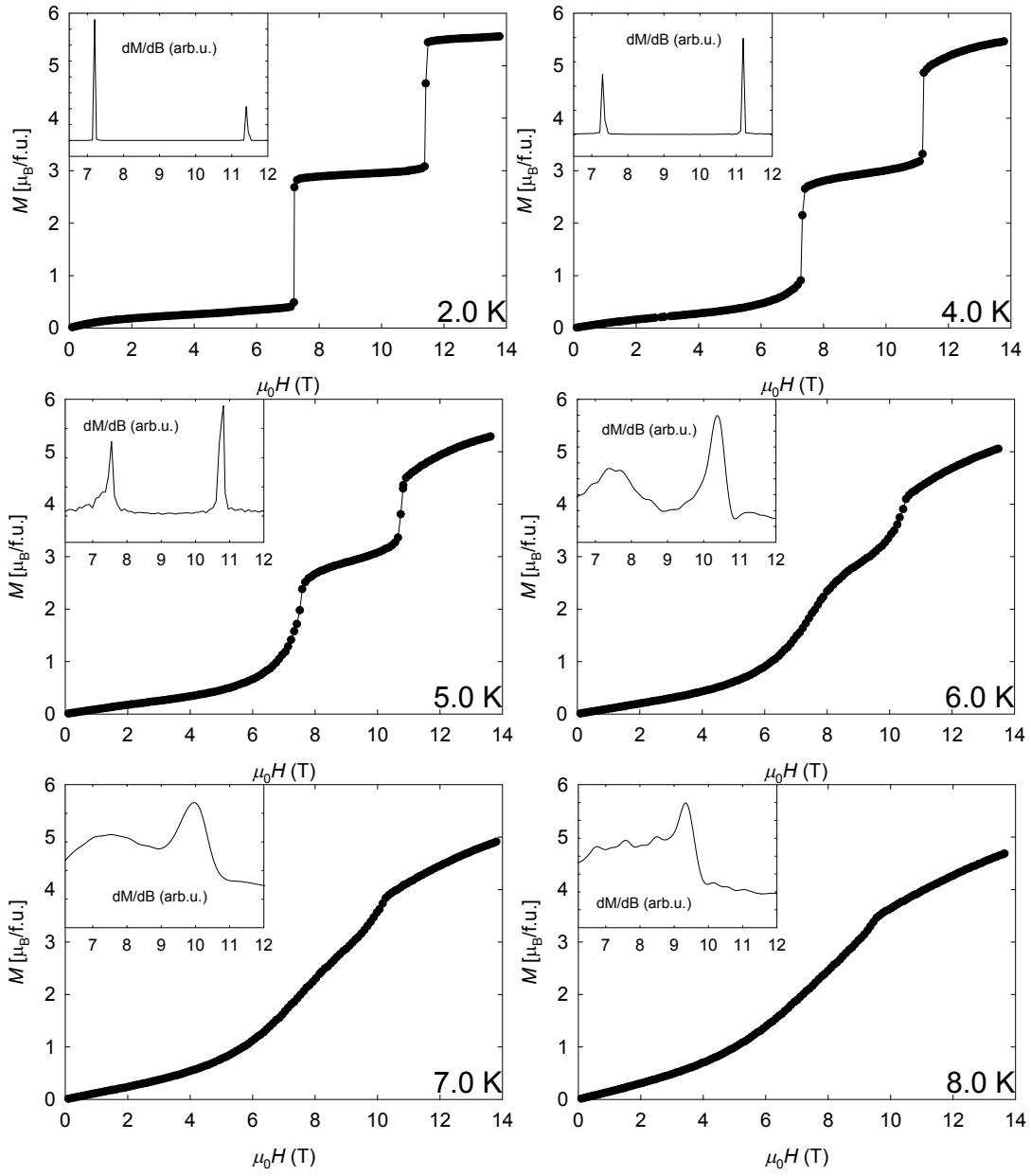

Figure 4.23: Nd_2IrIn_8 magnetization curves (part 1) with derivatives (ordered state) for $T = 2$ to 7 K. Two transitions are visible at low temperatures and become blurred at higher temperatures.

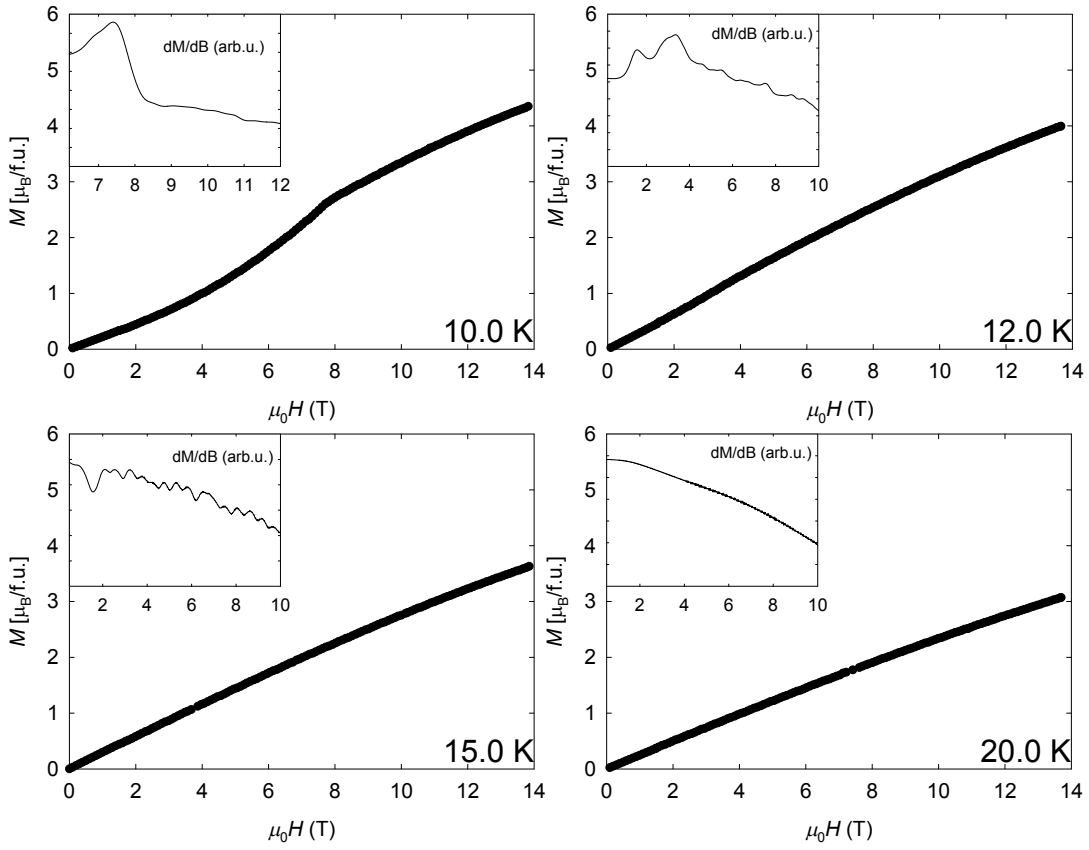

Figure 4.24: Nd_2IrIn_8 magnetization curves (part 2) with derivatives (ordered and paramagnetic state) for $T = 8$ to 20 K. One transition is still visible (at $T < T_N$).

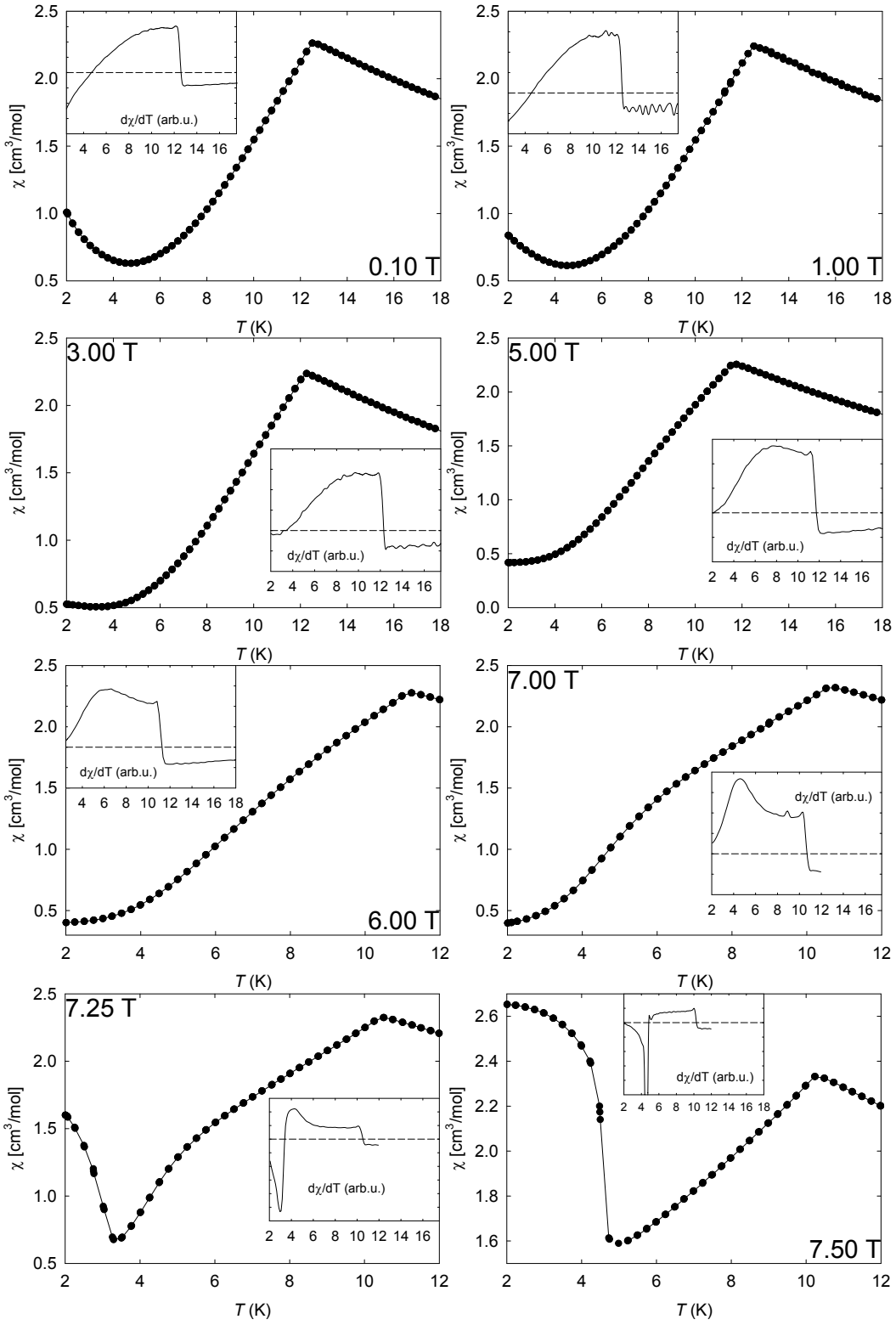

Figure 4.25: Nd_2IrIn_8 $M(T)$ curves (part 1) with derivatives for $\mu_0 H = 0.1$ T to 7.50 T. The PM to AFM transition is visible. A second transition emerges at fields higher than 7.25 T.

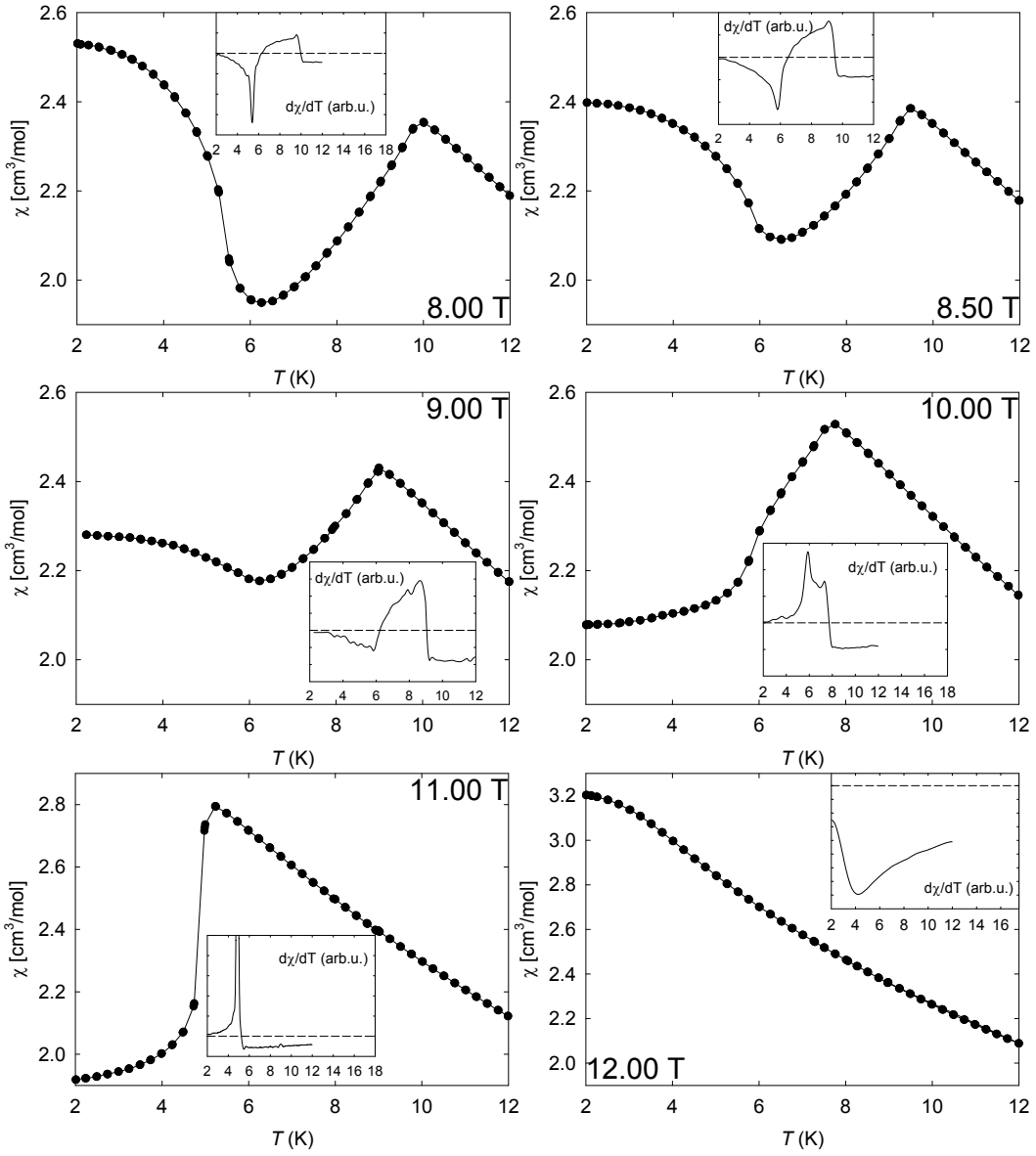

Figure 4.26: Nd_2IrIn_8 $M(T)$ curves (part 2) with derivatives for $\mu_0 H = 8.0$ T to 12.00 T. The PM to AFM transition is visible up to 11.0 T. The second transition up to 10.0 T.

0 K	14.4 K	91.5 K	106.4 K	141.3 K

Table 4.7: Obtained CEF energy levels

from the cubic law as seen from Figs. 4.28 and 4.29 and where the power of the dependency seems to be impossibly large. This behavior is believed to be due to the traces of $NdIn_3$ detected by EDX. Other evidence of a small amount of $NdIn_3$ could be two slightly elevated points on the $C_p(T)$ curve that would correspond to the transition temperatures 5.9 K and 5.3 K of $NdIn_3$ [11]. Figure 4.30 shows the magnetic specific heat up to 80 K. The magnetic entropy seems to increase to the expected value for Nd^{3+} ions $2R\ln(2J+1) = 2R\ln 10$. The magnetic entropy at T_N is considerably larger than $2R\ln 10$ which suggests a second doublet close to the ground-state doublet. The energy levels calculated from the CF parameters (Tab. 4.7) have the second lowest doublet at 14.4 K which could explain the increased entropy at TN. The Schottky specific heat calculated from the CF levels (see Tab. 2) is also in agreement with the data, as seen in Fig. 4.30.

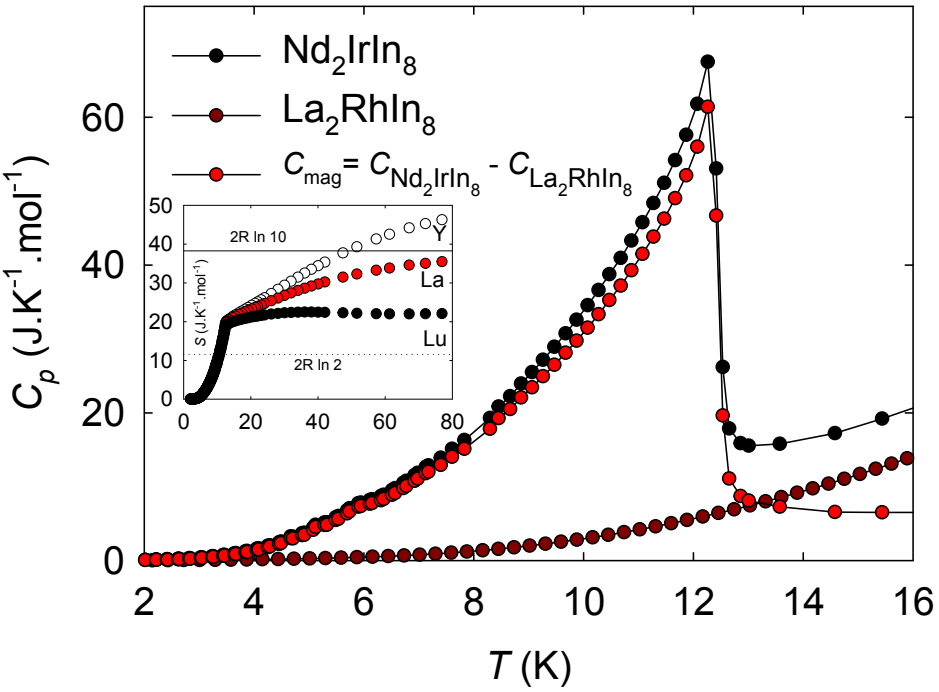

Figure 4.27: Low temperature specific heat for Nd_2IrIn_8, the subtracted specific heat of La_2RhIn_8 and the result. The inset shows temperature evolution of S_{mag} for different R_2RhIn_8 (R = Y, La, Lu) non-magnetic analogues used.

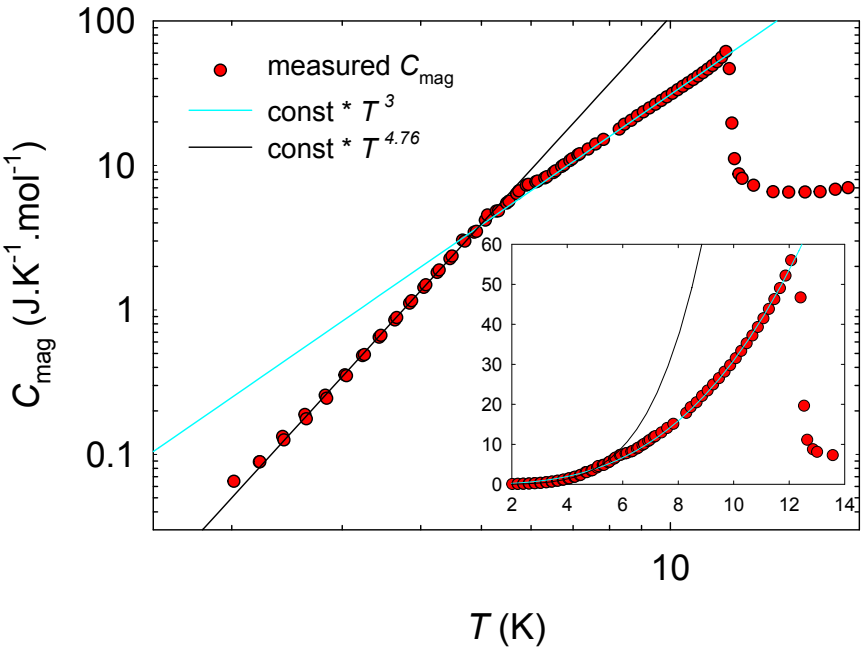

Figure 4.28: Log-log plot of the magnetic specific heat C_{mag} of Nd_2IrIn_8. The two parts of the curve below T_N have linear character on the plot which translates into relations of form $C = aT^k$. For anti-ferromagnetic magnons, $k = 3$ is expected which is in agreement in the upper part of the curve. The inset shows the plot in the normal scale.

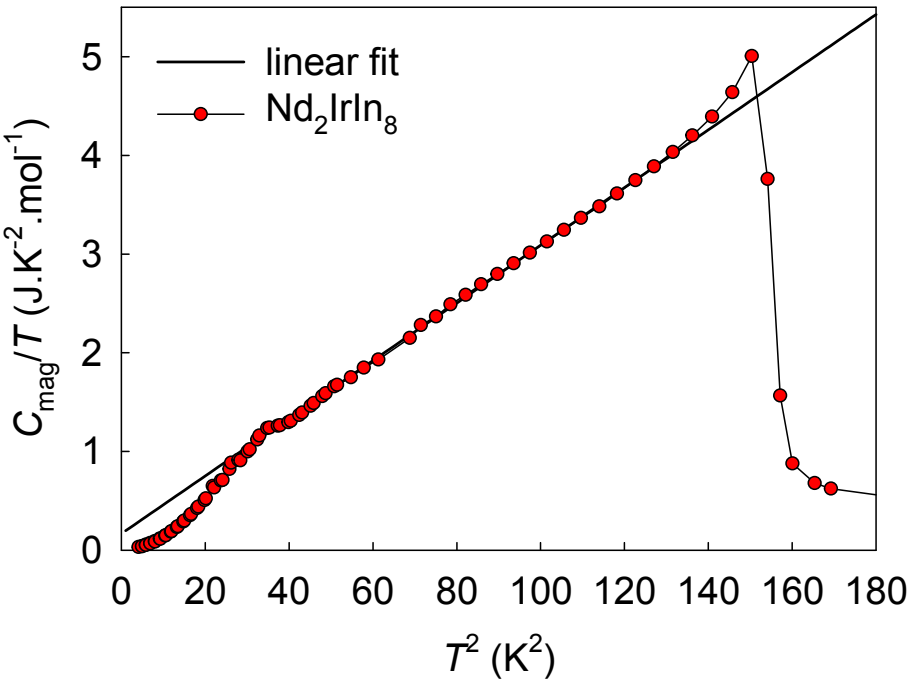

Figure 4.29: C_{mag}/T as a function of T^2. In this plot, the curve expected for the AF magnons is linear.

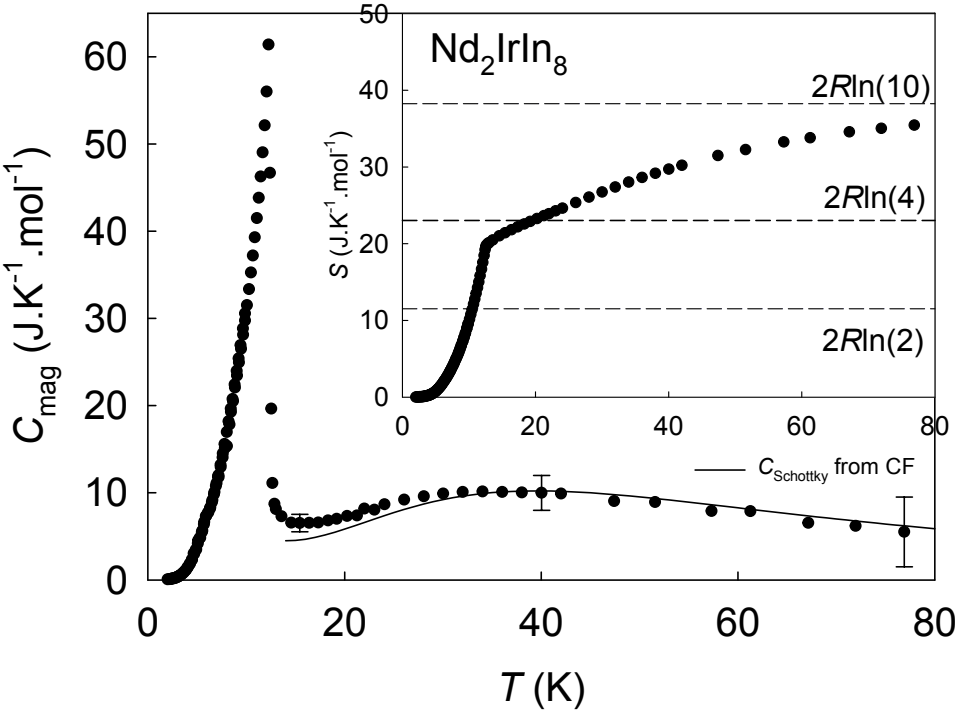

Figure 4.30: Magnetic specific heat at higher temperatures and comparison to the Schottky specific heat C_{Schottky} calculated from the CF parameters (Tab. 4.7).

Conclusion

The magnetic and thermodynamic properties of Nd_2RhIn_8 and Nd_2IrIn_8 compounds from the $R_mT_nX_{3m+2n}$ family have been studied in this thesis. We have also come up with a new interpretation of specific heat data of Nd_2IrIn_8 in the $T<T_N$ region and with comparison of measured data to crystal field calculations based on parameters obtained from an ab-initio method.

Single crystals of Nd_2RhIn_8 and Nd_2IrIn_8 were successfully grown from flux. The R_2TX_8 compounds crystallize in the Ho_2CoGa_8 tetragonal structure, space group *P4/mmm* (No. 123) and are antiferromagnetic with Néel temperatures 10.8(2) K, 12.5(2) K respectively. The measured susceptibility curves were fitted to the modified Curie-Weiss law. The magnetization curves at low temperatures (2 K) showed a step-like transitions, characteristic for this compound family, that become blurred and smeared at temperatures closer to T_N. The first derivative of magnetization curves was used to obtain the magnetic phase diagrams for field along the *c*-axis. The obtained magnetic phase diagrams are new results in the study of $R_mT_nX_{3m+2n}$ compounds. The expected similarity of the diagrams to those of related compounds and the presence of two phases was confirmed however we disproved the shape of the phase boundary presented by Duque et al. [37].

In the second part of our work, we built a program in the matrix calculator *Octave* for evaluation of properties based on the crystal field Hamiltonian which calculates CEF susceptibility and the Schottky specific heat for a set of CEF energy levels. The possibility to evaluate the Stevens operator equivalents directly from definition as a function of J has brought a significant simplification of the calculations compared to the need of using the tabulated values of $\hat{O}_n{}^m$.

Bibliography

[1] A. Tursina, S. Nesterenko, Y. Seropegin, H. Noël, and D. Kaczorowski. Ce_2PdIn_8, Ce_3PdIn_{11} and $Ce_5Pd_2In_{19}$—members of homological series based on $AuCu_3$- and $PtHg_2$-type structural units. *Journal of Solid State Chemistry*, 200:7 – 12, 2013.

[2] Zh.M. Kurenbaeva, E.V. Murashova, Y.D. Seropegin, H. Noël, and A.I. Tursina. The crystal structure of the new indide $CePt_2In_7$ from powder data. *Intermetallics*, 16(8):979 – 981, 2008.

[3] C Petrovic, P G Pagliuso, M F Hundley, R Movshovich, J L Sarrao, J D Thompson, Z Fisk, and P Monthoux. Heavy-fermion superconductivity in $CeCoIn_5$ at 2.3 K. *Journal of Physics: Condensed Matter*, 13(17):L337, 2001.

[4] G. Knebel, D. Braithwaite, P. C. Canfield, G. Lapertot, and J. Flouquet. Electronic properties of $CeIn_3$ under high pressure near the quantum critical point. *Phys. Rev. B*, 65:024425, Dec 2001.

[5] H. Hegger, C. Petrovic, E. G. Moshopoulou, M. F. Hundley, J. L. Sarrao, Z. Fisk, and J. D. Thompson. Pressure-induced superconductivity in quasi-2D $CeRhIn_5$. *Phys. Rev. Lett.*, 84:4986–4989, May 2000.

[6] M. Nicklas, V. A. Sidorov, H. A. Borges, P. G. Pagliuso, C. Petrovic, Z. Fisk, J. L. Sarrao, and J. D. Thompson. Magnetism and superconductivity in Ce_2RhIn_8. *Phys. Rev. B*, 67:020506, Jan 2003.

[7] J.D Thompson, R Movshovich, Z Fisk, F Bouquet, N.J Curro, R.A Fisher, P.C Hammel, H Hegger, M.F Hundley, M Jaime, P.G Pagliuso, C Petrovic, N.E Phillips, and J.L Sarrao. Superconductivity and magnetism in a new class of heavy-fermion materials. *Journal of Magnetism and Magnetic Materials*, 226–230, Part 1:5 – 10, 2001. Proceedings of the International Conference on Magnetism (ICM 2000).

[8] R. Movshovich, M. Jaime, J. D. Thompson, C. Petrovic, Z. Fisk, P. G. Pagliuso, and J. L. Sarrao. Unconventional superconductivity in $CeIrIn_5$ and $CeCoIn_5$: Specific heat and thermal conductivity studies. *Phys. Rev. Lett.*, 86:5152–5155, May 2001.

[9] A. Benoit, J.X. Boucherle, P. Convert, J. Flouquet, J. Palleau, and J. Schweizer. Magnetic structure of the compound $CeIn_3$. *Solid State Communications*, 34(5):293 – 295, 1980.

[10] N. D. Mathur, F. M. Grosche, S. R. Julian, I. R. Walker, D. M. Freye, R. K. W. Haselwimmer, and G. G. Lonzarich. Magnetically mediated superconductivity in heavy fermion compounds. *Nature*, 394:39, 1998.

[11] M. Amara, R.M. Galéra, P. Morin, J. Voiron, and P. Burlet. Magnetic phase diagram in $NdIn_3$. *Journal of Magnetism and Magnetic Materials*, 140:1157 – 1158, 1995.

[12] P. G. Pagliuso, J. D. Thompson, M. F. Hundley, and J. L. Sarrao. Crystal-field-induced magnetic frustration in $NdMIn_5$ and Nd_2MIn_8 (M=Rh, Ir) antiferromagnets. *Phys. Rev. B*, 62:12266–12270, Nov 2000.

[13] P. G. Pagliuso, J. D. Thompson, M. F. Hundley, J. L. Sarrao, and Z. Fisk. Crystal structure and low-temperature magnetic properties of R_mMIn_{3m+2} compounds (M=Rh or Ir; m =1,2; R =Sm or Gd). *Phys. Rev. B*, 63:054426, Jan 2001.

[14] Ya.M Kalychak. Composition and crystal structure of rare-earths–co–in compounds. *Journal of Alloys and Compounds*, 291(1–2):80 – 88, 1999.

[15] R. Lora-Serrano, L. Mendonça Ferreira, D.J. Garcia, E. Miranda, C. Giles, J.G.S. Duque, E. Granado, and P.G. Pagliuso. Structurally tuned magnetic properties of (;) intermetallic antiferromagnets. *Physica B: Condensed Matter*, 384(1–2):326 – 328, 2006. LAW3M-05Proceedings of the Seventh Latin American Workshop on Magnetism, Magnetic Materials and their Applications.

[16] P Čermák, M Kratochvílová, K Pajskr, and P Javorský. Magnetic phase diagrams of R_2RhIn_8 (R = Tb, Dy, Ho, Er and Tm) compounds. *Journal of Physics: Condensed Matter*, 24(20):206005, 2012.

[17] Nguyen Van Hieu, Tetsuya Takeuchi, Hiroaki Shishido, Chie Tonohiro, Tsutomu Yamada, Hiroshi Nakashima, Kiyohiro Sugiyama, Rikio Settai, Tatsuma D. Matsuda, Yoshinori Haga, Masayuki Hagiwara, Koichi Kindo, Shingo Araki, Yasuo Nozue, and Yoshichika Ōnuki. Magnetic properties and crystalline electric field scheme in $RRhIn_5$ (R: Rare Earth). *Journal of the Physical Society of Japan*, 76(6):064702, 2007.

[18] G. Arnold and N. Nereson. Magnetic properties of dypt3 and dyin3. *The Journal of Chemical Physics*, 51(4):1495–1499, 1969.

[19] A. Czopnik, H. Mädge, and B. Staliński. Specific heat of hoin3, and erin3 compounds. *physica status solidi (a)*, 94(1):K13–K16, 1986.

[20] A.F. Deutz, H.B. Brom, W.J. Huiskamp, L.J. de Jongh, and K.H.J. Buschow. Magnetic properties of the antiferromagnetic compound tmin3. *Journal of Magnetism and Magnetic Materials*, 78(1):31 – 39, 1989.

[21] Robin T. Macaluso, J. L. Sarrao, N. O. Moreno, P. G. Pagliuso, J. D. Thompson, Frank R. Fronczek, M. F. Hundley, A. Malinowski, , and Julia Y. Chan. Single-crystal growth of Ln_2MIn_8 (Ln = La, Ce; M = Rh, Ir):Implications for the heavy-fermion ground state. *Chemistry of Materials*, 15(6):1394–1398, 2003.

[22] S. Ohara, I. Sakamoto, T. Shomi, and G. Chen. Magnetic and transport properties of R_2MIn_8 (R=La Ce Pr, M=Rh In). *Acta Physica Polonica B*, 34:1243, 2003.

[23] N.W. Ashcroft and N.D. Mermin. *Solid state physics*. Saunders College Publishing, 1976.

[24] K.W.H. Stevens. *Proc. Phys. Soc. (London)*, A65:209, 1952.

[25] J.M.D. Coey. *Magnetism and Magnetic materials*. Cambridge University Press, 2009.

[26] C. Kittel. *Úvod do fyziky pevných látek*. 1. vydání. Academia, Praha, 1985.

[27] P. Čermák, K. Uhlířová, and P. Javorský. Specific heat of a $CeCu_{0.7}Al_{3.3}$ single crystal. *Physica B: Condensed Matter*, 405(9):2294 – 2296, 2010.

[28] Fullprof. Webpage. `https://www.ill.eu/sites/fullprof/`. January 2016.

[29] Octave. Octave webpage. `https://www.gnu.org/software/octave/`. March 2016.

[30] C A Martin. Simple treatment of anharmonic effects on the specific heat. *Journal of Physics: Condensed Matter*, 3(32):5967, 1991.

[31] P. Čermák, M. Diviš, M. Kratochvílová, and P. Javorský. Specific heat study of R_2RhIn_8 (R=Y, La, Lu) compounds. *Solid State Communications*, 163:55 – 59, 2013.

[32] Devang A. Joshi, R. Nagalakshmi, S. K. Dhar, and A. Thamizhavel. Anisotropic magnetization studies of R_2CoGa_8 single crystals (R=Gd, Tb, Dy, Ho, Er, Tm, Y, and Lu). *Phys. Rev. B*, 77:174420, May 2008.

[33] Petr Čermák, Karel Prokeš, Bachir Ouladdiaf, Martin Boehm, Marie Kratochvílová, and Pavel Javorský. Magnetic structures in the magnetic phase diagram of Ho_2RhIn_8. *Phys. Rev. B*, 91:144404, Apr 2015.

[34] M.T. Hutchings. Point-charge calculations of energy levels of magnetic ions in crystalline electric fields. volume 16 of *Solid State Physics*, pages 227 – 273. Academic Press, 1964.

[35] K. Pajskr, P. Javorský, M. Diviš, J. Zubáč, and K. Vlášková. Low-temperature magnetic phase diagram and specific heat of Nd_2IrIn_8. *Physica B: Condensed Matter*, 483:94 – 98, 2016.

[36] P. Javorský, K. Pajskr, M. Klicpera, P. Čermák, Y. Skourski, and A.V. Andreev. High-field magnetization and magnetic phase diagrams in Nd_2RhIn_8 and Tb_2RhIn_8. *Journal of Alloys and Compounds*, 598:278 – 281, 2014.

[37] J.G.S. Duque, R. Lora Serrano, D.J. Garcia, L. Bufaical, L.M. Ferreira, P.G. Pagliuso, and E. Miranda. Field induced phase transitions on $NdRhIn_5$ and Nd_2RhIn_8 antiferromagnetic compounds. *Journal of Magnetism and Magnetic Materials*, 323(7):954 – 956, 2011.

[38] Devang A. Joshi, R. Nagalakshmi, S. K. Dhar, and A. Thamizhavel. Anisotropic magnetization studies of R_2CoGa_8 single crystals (R=Gd, Tb, Dy, Ho, Er, Tm, Y, and Lu). *Phys. Rev. B*, 77:174420, May 2008.

[39] Petr Čermák, Pavel Javorský, Marie Kratochvílová, Karel Pajskr, Milan Klicpera, Bachir Ouladdiaf, Marie-Hélène Lemée-Cailleau, Juan Rodriguez-Carvajal, and Martin Boehm. Magnetic structures of non-cerium analogues of heavy-fermion Ce_2RhIn_8: The case of Nd_2RhIn_8, Dy_2RhIn_8 and Er_2RhIn_8. *Phys. Rev. B*, 89:184409, May 2014.

[40] M. Diviš, J. Rusz, H. Michor, G. Hilscher, P. Blaha, and K. Schwarz. Magnetic properties of $NdNi_2B_2C$ from first principles calculations. *Journal of Alloys and Compounds*, 403(1–2):29 – 33, 2005.

[41] K. Schwarz, P. Blaha, and G.K.H. Madsen. Proceedings of the europhysics conference on computational physics computational modeling and simulation of complex systems electronic structure calculations of solids using the WIEN2k package for material sciences. *Computer Physics Communications*, 147(1):71 – 76, 2002.

List of Figures

List of Tables

Octave scripts

Notes: every function needs to be put in a separate .m file with the function name or a script file with multiple functions has to be used. Only the $\hat{O}_2{}^0$ and $\hat{O}_4{}^0$ are shown below. The rest, ie. the $\hat{O}_4{}^4$,$\hat{O}_6{}^0$ and $\hat{O}_6{}^4$ operators can be constructed in a straightforward fashion.

Heat Capacity

```
% function y = einstein(T,T_E)
% Returns Einstein heat capacity for input T and Einstein temp T_E
% (Accepts arrays of T)
function y = einstein(T,T_E)
   R = 8.31;
   x_E = T_E./T;
   pom = exp(x_E);
   y =  R .* x_E .* x_E .* pom ./ ((pom - 1).**2);
end

% function y = debye(T,T_D)
% returns C_Debye for T and Debye temp T_D
% (accepts arrays of T)
function y = debye(T,T_D)
   R = 8.314;
   x_D = T_D./T;
   q = zeros(size(T));
   for iii = 1:length(q)
      q(iii) = quad(@fceinteg,0,x_D(iii));
   endfor
   y = 3 * R ./ (x_D .**3) .* q;
end

%numericaly integrated function in debye
function y = fceinteg(x)
   pom = exp(x);
   y = (x**4) * pom / ((pom - 1)**2);
end

%Calculates the Schottky heat capacity
function y = hc_a(T,levels);
   T = T(:);
   levels = levels(:);

   pom1= exp(-levels * (1./T)');
   pom2 = ones(size(levels)) * sum(pom1);
   pom1 = pom1 ./ pom2;

   y = 8.314 * ((levels .* levels)' * pom1
```

```
      - (levels' * pom1).^2) ./ T' ./T';
endfunction
```

CEF susceptibility

```
function y = J_x(J,conv = 1)
   y = .5 * (J_plus(J,conv) + J_minus(J,conv));
end

function y = J_y(J,conv = 1)
   y = .5/i*(J_plus(J,conv) - J_minus(J,conv));
end

function y = J_z(J,conv=1)
   y = diag(linspace(conv * J,conv * (-J),2*J+1));
end

function y = J_plus(J,conv = 1)
   p1 = linspace(-J,J-1,2*J);
   p1 = sqrt(J*(J+1) - p1.*(p1+1));
   y = diag(p1,conv);
end

function y = J_minus(J,conv = 1)
   y = J_plus(J,conv)';
end

function y = O_20(J,conv = 1)
   JJ = J*(J+1);
   J2p1 = 2*J + 1;

   Jz = J_z(J,conv);
   E = eye(J2p1);

   y = 3*Jz*Jz - JJ * E;
end

function y = O_40(J,conv = 1)
JJ = J*(J+1);
J2p1 = 2*J + 1;

Jz = J_z(J,conv);
E = eye(J2p1);

y = 35 * Jz**4 + (25 - 30 * JJ)*Jz**2 + E * JJ * (3 * JJ - 6);
end
```

```
function [J J2p1 gJ Alpha Beta Gamma] = ion_p(s)
   switch s
      case {"Nd","ND","Nd3+"}
M = [4.5 8.0/11.0 -7.0/1089.0 -136.0/467181.0 -1615.0/42513471.0];
      case {"Ce","CE","Ce3+"}
         M = [2.5 6.0/7.0 -2.0/35.0 2.0/315.0 0];
      otherwise
         M = zeros(1,5);
   endswitch
J = M(1); J2p1 = 2*M(1) + 1; gJ = M(2);
Alpha = M(3); Beta = M(4); Gamma=M(5);
end

function  y = susc_CEF(ion,B,H,T,rec = 1)
   % results are in u_B / T (or T/u_B when rec is 1)
   uB = 0.67171;  % in K/T
   [J J2p1 gJ Alpha Beta Gamma] = ion_p(ion);
   y=zeros(size(T));
   p1 = ones(J2p1,1);
   Jz = J_z(J); Jx = J_x(J); Jy = J_y(J);

   H_size = sqrt(H*H');
   H_dir = H / H_size;

   hamiltonian = B(1) * O_20(J) + B(2) * O_40(J) + ...
      B(3)* O_44(J) + B(4) * O_60(J) + B(5) * O_64(J);
   [U,E] = eig(hamiltonian);
   energie= p1'*E;
   energie = energie - min(energie);

   JH = H_dir(1) * Jx + H_dir(2) * Jy + H_dir(3)*Jz;
   JH = U' * JH * U;
   E_n = p1*energie;
   E_m = E_n';

   denominator = E_m - E_n;
   nuly = all(abs(denominator) < 1e-7,J2p1);
   denominator = denominator + nuly;
   for jj = 1:length(T)
      prst = exp(-energie/T(jj));
      Z = prst*p1;
      CH = prst*abs(diag(JH)).**2 /T(jj);
      numerator    = exp(-E_n/T(jj)) - exp(-E_m/T(jj));
      limita     = nuly.*exp(-E_m/T(jj))/T(jj);
      numerator += limita;
      frac = numerator./denominator;
      frac = frac - diag(diag(frac));
```

```
      CH += p1'*(abs(JH).**2 .*frac)*p1;
      CH = CH/Z;
      y(jj) = CH;
   endfor
   y = gJ*gJ*uB*y;
   if (rec == 1)
      y = 1./y;
   end
end
```